

The 2021 Loyalty Island earthquake (Mw 7.7): tsunami waveform inversion and implications for tsunami forecasting for New Zealand

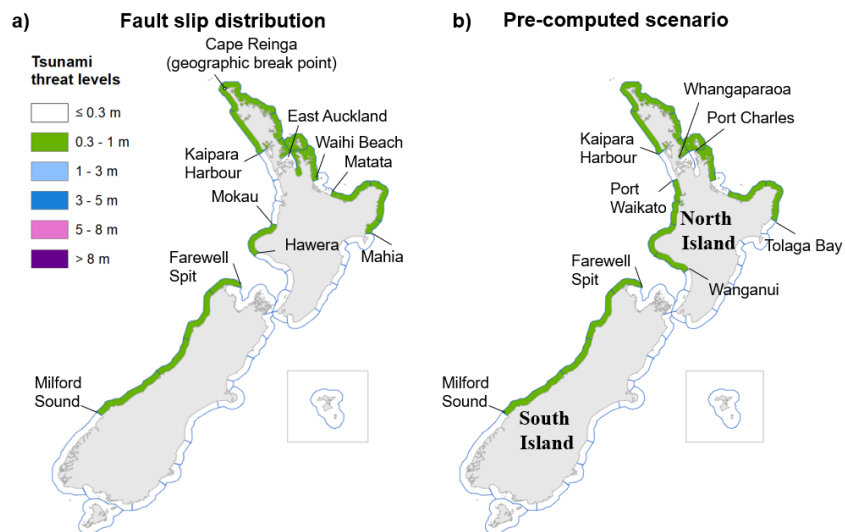
Aditya Riadi Gusman¹, Jean Roger¹, William Power¹, and Bill Fry¹

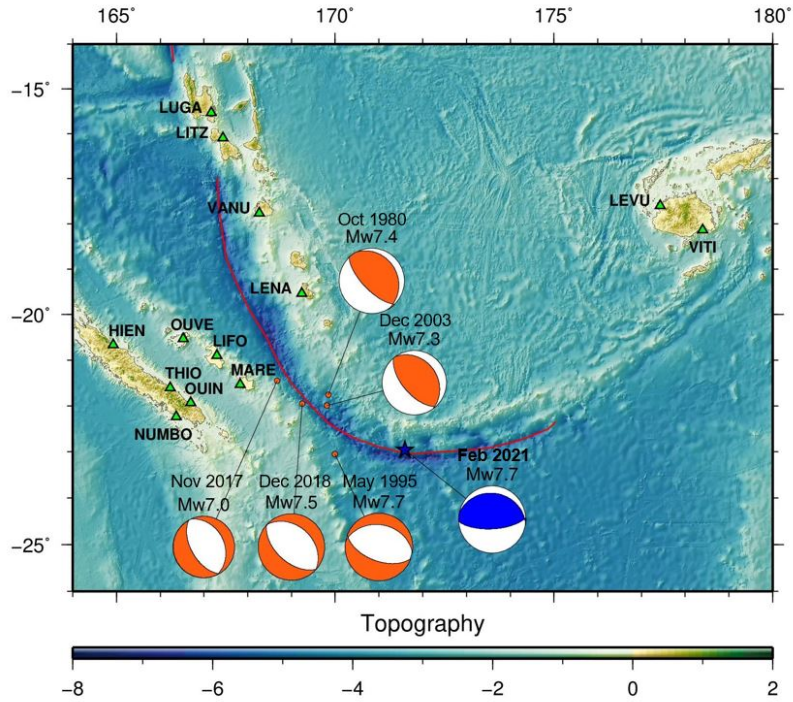
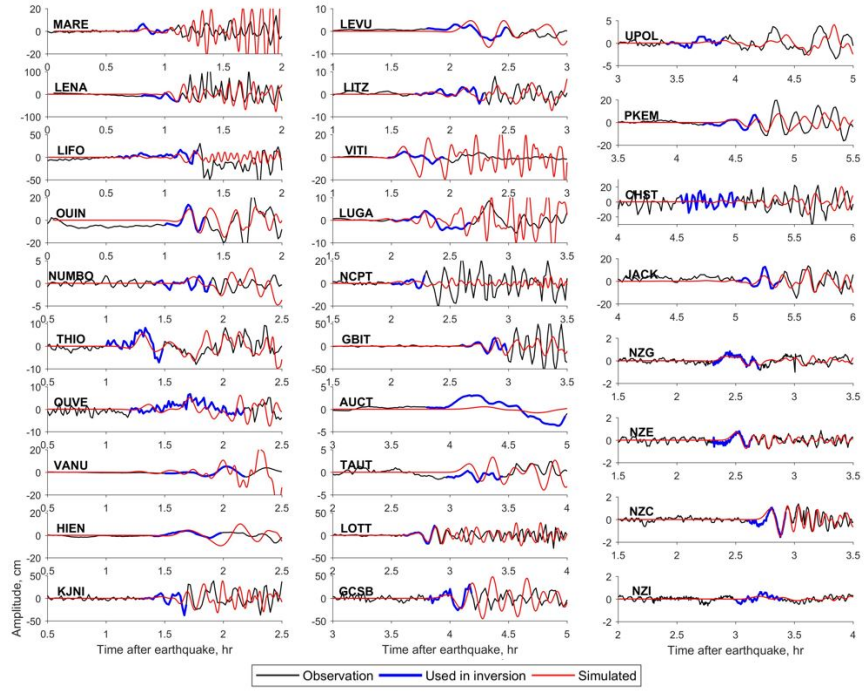
¹GNS Science

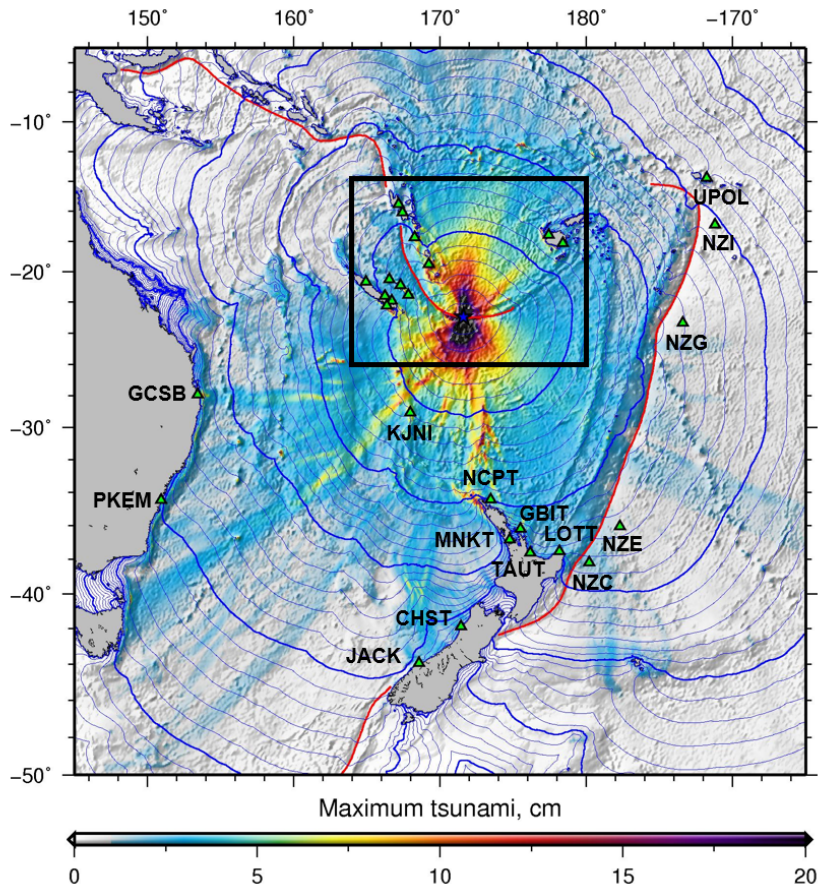
November 22, 2022

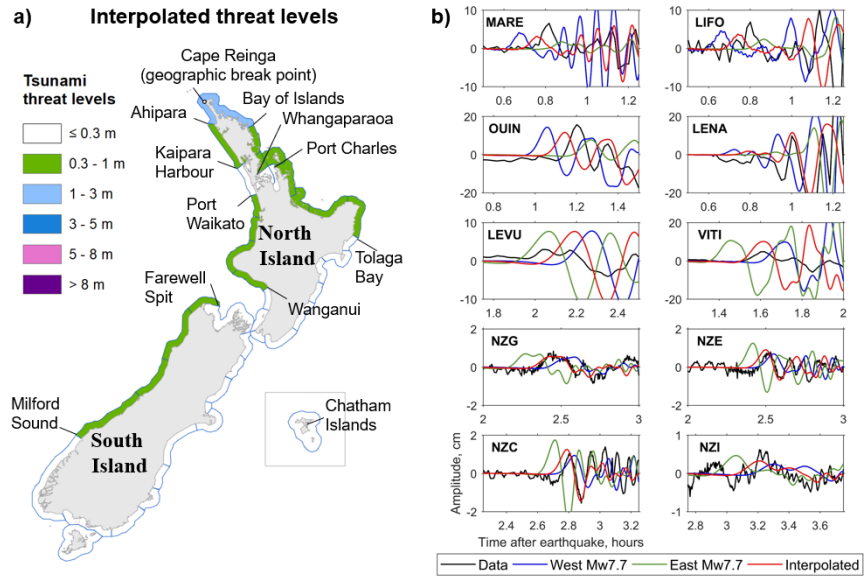
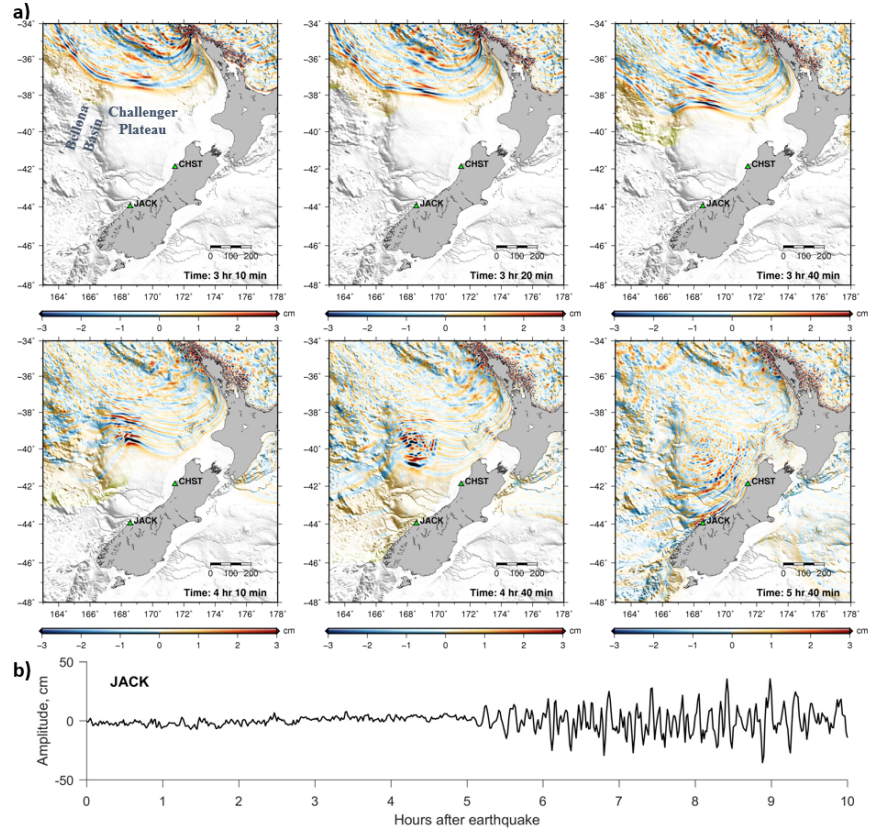
Abstract

A tsunamigenic earthquake with thrust faulting mechanism occurred off the Loyalty Islands, New Caledonia, in the Southern New Hebrides subduction zone on the 10th of February 2021. The tsunami was observed at coastal gauges in the surrounding islands and in New Zealand. The tsunami was also recorded at a new DART network that was designed to enhance the tsunami forecasting capability of the Southwestern Pacific. We used the tsunami waveforms in an inversion to estimate the fault slip distribution. The estimated major slip region is located near the trench with maximum slip amount of 4 m. The computed seismic moment for the source model of 3.39×10^{20} Nm (Mw 7.65) is slightly smaller than the Global Centroid Moment Tensor or USGS W-phase Moment Tensor solutions. We evaluate two tsunami forecasting approaches of selecting a pre-computed scenario and interpolating pre-computed scenarios for coastal regions in New Zealand. For the evaluation, we first computed the tsunami threat levels in New Zealand coastal regions from the earthquake source model to make a reference threat level map. The results show that the tsunami threat level maps from a pre-computed Mw 7.7 scenario located closest to the epicenter and from an interpolation of two scenarios matched the reference threat levels at most of the coastal regions. We also report on utilization of the coastal gauge and DART buoy data for updating forecasts in real-time during the event and discuss the differences between the rapid-response forecast and post-event retrospective forecasts.









1 **The 2021 Loyalty Island earthquake (Mw 7.7): tsunami waveform**
2 **inversion and implications for tsunami forecasting for New**
3 **Zealand**

4

5 Aditya Riadi Gusman, Jean Roger, William Power, and Bill Fry

6 GNS Science, Lower Hutt, New Zealand

7 (a.gusman@gns.cri.nz)

8

9 **Key Points:**

- 10 • Significant near trench slip on the plate interface of the 2021 Loyalty Island earthquake
11 was estimated by inverting tsunami waveforms at coastal and offshore stations.
- 12 • Accurate tsunami forecast can be obtained from interpolating results of precomputed
13 earthquake scenarios.
- 14 • The new New Zealand DART network is essential in improving the tsunami warning
15 capability for countries in the South West Pacific.

16 **Abstract**

17 A tsunamigenic earthquake with thrust faulting mechanism occurred off the Loyalty
18 Islands, New Caledonia, in the Southern New Hebrides subduction zone on the 10th of February
19 2021. The tsunami was observed at coastal gauges in the surrounding islands and in New
20 Zealand. The tsunami was also recorded at a new DART network that was designed to enhance
21 the tsunami forecasting capability of the Southwestern Pacific. We used the tsunami
22 waveforms in an inversion to estimate the fault slip distribution. The estimated major slip

23 region is located near the trench with maximum slip amount of 4 m. The computed seismic
24 moment for the source model of 3.39×10^{20} Nm (Mw 7.65) is slightly smaller than the Global
25 Centroid Moment Tensor or USGS W-phase Moment Tensor solutions. We evaluate two
26 tsunami forecasting approaches of selecting a pre-computed scenario and interpolating pre-
27 computed scenarios for coastal regions in New Zealand. For the evaluation, we first computed
28 the tsunami threat levels in New Zealand coastal regions from the earthquake source model to
29 make a reference threat level map. The results show that the tsunami threat level maps from a
30 pre-computed Mw 7.7 scenario located closest to the epicenter and from an interpolation of
31 two scenarios matched the reference threat levels at most of the coastal regions. We also report
32 on utilization of the coastal gauge and DART buoy data for updating forecasts in real-time
33 during the event and discuss the differences between the rapid-response forecast and post-event
34 retrospective forecasts.

35

36 **Plain language summary**

37 We estimated the tsunami source of the 2021 Loyalty Island earthquake from inversion
38 of tsunami waveforms recorded at offshore DART and coastal stations. These DART stations
39 are part of a new DART network that was designed to enhance the tsunami forecasting
40 capability of New Zealand and the Southwestern Pacific region. The inversion result suggest
41 that the earthquake ruptured the plate interface with relatively large slip near the trench. Our
42 source model can explain the observed tsunami and its general slip distribution pattern is
43 consistent with another independent earthquake source study from USGS that used teleseismic
44 waveforms. The tsunami threat level map for New Zealand coastal regions produced from the
45 source model is then used as a reference map to evaluate two techniques for rapid tsunami
46 forecasting. Both techniques utilize pre-computed earthquake scenarios. The first technique is
47 using the epicenter and magnitude of the earthquake to select the nearest earthquake scenario.

48 The second technique interpolates pre-computed results of two earthquake scenarios around
49 the epicenter. The tsunami hindcast accuracies from the two techniques are high as the resulting
50 tsunami threat levels matched the reference ones at most of the warning regions in New Zealand.

51

52 **Keywords:** Tsunami waveform inversion, the 2021 Loyalty Island earthquake, Southern New
53 Hebrides/Vanuatu Subduction Zone, tsunami forecast, earthquake source model

54

55 **1. Introduction**

56 One of subduction zones in the Pacific Ocean that poses tsunami threats to New Zealand
57 and other southwest Pacific states is the New Hebrides (also known as Vanuatu) subduction
58 zone. In this region, thrust earthquakes occur on the plate interface between the subducting
59 Australia plate and the overriding New Hebrides arc and North Fiji Basin (Calmant et al., 2003).
60 On the 10th of February 2021, a magnitude (M_w) 7.7 earthquake occurred in this subduction
61 zone and generated a tsunami (Figure 1). Based on the earthquake's magnitude, location and
62 depth, a tsunami warning was issued by the Pacific Tsunami Warning Center (PTWC) for
63 island nations around the epicenter in the South West Pacific such as New Caledonia, Fiji,
64 Vanuatu, Tonga, New Zealand, and Australia. The National Emergency Management Agency
65 (NEMA) of New Zealand issued tsunami threat warnings for several coastal regions in the
66 country.

67 According to the United States Geological Survey (USGS), the earthquake occurred at
68 13:19:55 UTC with a hypocenter located at 23.054° S - 171.601° E and 10 km depth
69 southeastward of the Loyalty Islands archipelago in the southern part of the New Hebrides
70 subduction zone. It is located to the east of the region where the Loyalty Ridge, part of the
71 Australian Plate, is subducted under the overriding Pacific Plate at a convergence rate of ~12
72 cm/yr and where Mw7.0+ tsunamigenic earthquakes occurred during the last century (Roger

73 et al., *subm.*). Since the May 17, 1995 Mw 7.7 Walpole tsunamigenic earthquake, the New
74 Hebrides subduction zone, which is amongst the most seismically active, has produced at least
75 12 small (amplitude < 50 cm) to moderate (0.5 m < amplitude < 5 m) tsunamis. These tsunamis
76 were triggered by earthquakes, such as the November 19, 2017 Mw 7.0 earthquake or the recent
77 December 5, 2018 Mw 7.5 Tadiné earthquake (Figure 1) whose maximum amplitude reached
78 more than 2 m in New Caledonia and 4 m in Aneityum Island, Vanuatu (Sahal et al., 2010;
79 Roger et al., 2019; Roger et al., 2021). Although the central and northern part of the New
80 Hebrides subduction zone is also known to have experienced tsunamis triggered by even larger
81 earthquakes of Mw 8.0+ (Ioualalen et al., 2017), there is no clear evidence for Mw8.0+
82 earthquakes in the southeasternmost part of the subduction zone (170°E-175°E), where the
83 February 10, 2021 earthquake occurred. Lack of recorded large events may also have a physical
84 explanation. In this region, the convergence is no longer eastward verging, as is the case for
85 the rest of the subduction zone, but instead oriented N17°E perpendicular to the trench with a
86 rate measured at ~5 cm/yr, making it the slowest converging part of the New Hebrides
87 convergence zone (Calmant et al., 2003). For comparison, the subduction convergence rate
88 north of 22°S is ~12 cm/yr.

89 The focal mechanisms provided by the Global Centroid Moment Tensor (GCMT) and
90 USGS W-phase moment tensor (WMT) solutions suggest that the earthquake ruptured the plate
91 interface with a nearly pure thrusting mechanism. The GCMT solution gives a seismic moment
92 of 4.01×10^{20} Nm and nodal planes with strike = 279°/87°, dip = 23°/67°, and rake = 101°/85°.
93 The USGS WMT solution gives a seismic moment of 4.36×10^{20} Nm and nodal planes with
94 strike = 246°/92°, dip = 17°/75°, and rake = 65°/97°. The USGS finite fault model for the thrust
95 faulting event maps earthquake rupture all the way to the trench with moment rate maximum
96 at 15 s after earthquake origin time and rupture termination within 40 s.

97 This geometry of nearly pure thrusting earthquakes can trigger tsunamis with a main energy
98 axis orientation of South-Southwest/North-Northeast, i.e. toward New Zealand and
99 Southeastern Australia to the south and toward Vanuatu to the north (Okal, 1988). Thus, the
100 tsunami from the 2021 Loyalty Island earthquake propagated in the southwestern region of the
101 Pacific Ocean, and was recorded at local coastal gauges in New Caledonia and Vanuatu, and
102 also at regional distances in places like Fiji, Western Samoa, Tuvalu, Australia (including
103 Tasmania) and New Zealand, more than 3000 km away from the earthquake epicenter (Figure
104 1 and Figure 2 and Table 1). The tsunami was also recorded by the New Zealand network of
105 DART buoys in the Hikurangi-Kermadec-Tonga subduction zone (Figure 2)(Fry et al., 2020).
106 Deployment of this network was started by the government of New Zealand in December 2019
107 (DART NZA, B, C, E, and F) and September 2020 (DART NZG, H, and I) and is scheduled to
108 be finished in 2022 (DART NZD, J, K, and L) (Power et al., 2018). It was designed to enhance
109 the capability of New Zealand and other Pacific states to detect and forecast tsunamis in the
110 Southwestern Pacific and was strongly motivated by the recognized gap in operational response
111 to events occurring at regional propagation distances (Fry et al., 2018).

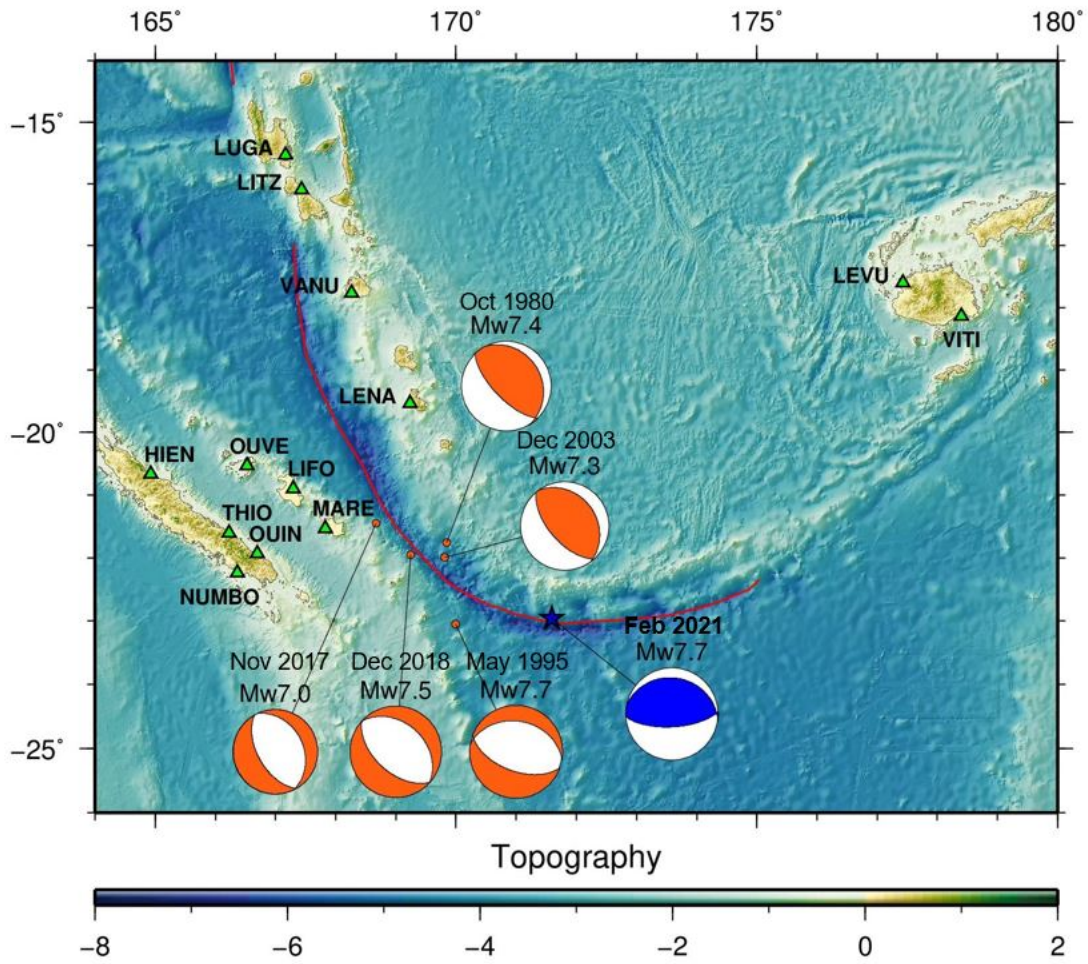
112 The procedures for tsunami early warning in New Zealand make use a two-stage approach
113 involving initial issuance of “action maps” and subsequent “threat maps”. The action maps are
114 based on highly uncertain early earthquake and magnitude estimates. They are designed to
115 rapidly and conservatively assess the possibility of land threat and trigger activation of
116 emergency response. They are binary maps, assigning “land threat” or “under assessment” to
117 coastal zones. This early forecast is based on pre-computed tsunami scenarios and simple 1D
118 tsunami prediction equations (Power, 2017). Following refinement of earthquake source
119 parameters, typically derived through available w-phase moment tensor inversions,
120 precomputed tsunami scenarios from earthquake sources located in subduction zones around
121 the Pacific Ocean are used to issue forecast maps. Forecast maps include tsunami amplitude

122 information. The precomputed tsunami scenario catalogue contains a total of ~1000 uniform
123 fault slip models with earthquake magnitudes ranging from 6.9 to 9.3 (Gusman et al., 2019). A
124 tsunami threat level map for coastal regions in New Zealand was prepared for every earthquake
125 scenario. Pre-computed tsunami waveforms at coastal gauges and DART buoys are available
126 too. In this database, there is a scenario available with the same magnitude and a location very
127 close to the 2021 Loyalty Island earthquake.

128 Facing the enduring threat of tsunamis affecting their coastal populations and
129 infrastructures, many countries have built tsunami pre-computed scenarios databases to support
130 tsunami preparation and response, for example Japan (Tatehata, 1997; Hoshihara and Ozaki,
131 2014), French Polynesia (Reymond et al., 2012), Turkey (Onat and Yalciner, 2013), Australia
132 (Greenslade et al., 2011), Indonesia (Harig et al., 2019), Portugal (Matias et al., 2012), New
133 Caledonia (Duphil et al., 2021). High resolution tsunami inundation forecasting through
134 scenario selection of pre-computed scenarios, or deep learning using pre-computed scenarios,
135 have also been considered (Gusman et al., 2014; Mulia et al., 2018; Mulia et al., 2020). Ways
136 to improve the use of those databases, and the accuracy of impact forecasting, especially for
137 scenarios whose magnitude or location lie outside the ranges of the existing ones, are of major
138 interest.

139 In this paper, the tsunami waveforms recorded at coastal gauges and DART stations are
140 used in an inversion process to estimate the non-uniform fault slip distribution of the
141 earthquake. The tsunami threat level map in New Zealand made from the earthquake source
142 model was then used as a reference map (true state) to evaluate our tsunami forecasting
143 approach. We compare the reference threat level map with the map for the nearest scenario
144 with Mw 7.7 to the epicenter. We also evaluate a map created by interpolating the result from
145 two Mw 7.7 scenarios around the epicenter. Here we describe the interpolation method to
146 produce an interpolated threat level map and tsunami waveforms at observation points. Finally,

147 we discuss the effectiveness of the pre-computed scenarios for providing accurate tsunami
148 forecasts for New Zealand coastal regions. We conclude by describing response forecast
149 calibration based on data from coastal tide gauges and DART stations.

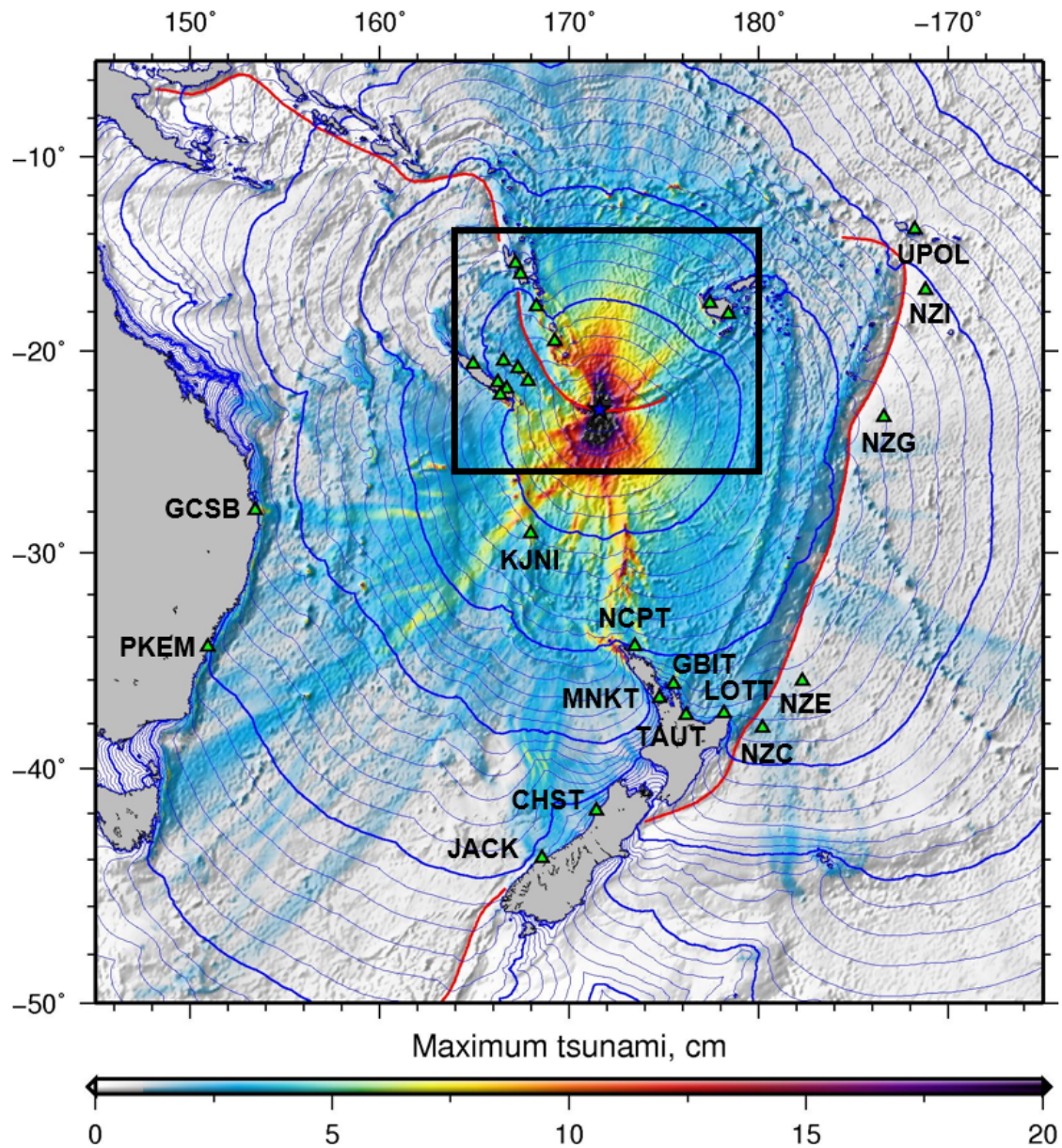


150

151

152 *Figure 1 Major tsunamigenic earthquakes in the New Hebrides subduction zone from 1980. Focal*
153 *mechanisms are based on GCMT solutions. Green triangles indicate coastal gauges at which the*
154 *tsunami waveforms used in this study were recorded. Convergent plate boundaries are indicated by red*
155 *lines.*

156



157

158 *Figure 2 Theoretical tsunami maximum amplitude and travel time from the epicenter calculated using*
 159 *bathymetry data from the 2021 Loyalty Island earthquake source model. Thick blue contour lines*
 160 *indicate time intervals of 1 hour, while thin blue contour lines indicate time intervals of 10 minutes.*
 161 *Green triangles indicate coastal gauges and DART stations at which the tsunami waveforms used in*
 162 *this study were recorded. Plate boundaries are indicated by red lines. Stations names for the green*
 163 *triangles inside the black rectangle can be seen in Figure 1.*

164

165 **2. Tsunami waveform and bathymetric data**

166 *2.1. Tsunami waveforms*

167 The tsunami generated by the 2021 Loyalty Island earthquake was clearly recorded at
 168 coastal gauges in New Caledonia, Vanuatu, Fiji, Australia, Samoa, and New Zealand. The
 169 coastal gauge records were available from the IOC water level monitoring website
 170 (<http://www.ioc-sealevelmonitoring.org>). We removed the tides using a polynomial fit method
 171 to obtain the tsunami waveforms. The tsunami was also recorded at DART buoys NZC, NZE,
 172 NZG, and NZI which are located seaward of the Hikurangi-Kermadec-Tonga subduction zone
 173 trench (Figure 2). We also removed the tides recorded at the DARTs by the polynomial fit
 174 method. Then high frequency waves were removed using a low pass filter with cutoff period
 175 of 200 sec to get the tsunami waveforms.

176

177 Table 1. Coastal gauge and DART station information and the tsunami records sorted by distance from epicentre

178

Station Code	Location	Country/Region	Longitude	Latitude	Distance from epicenter (km)	First wave amplitude (cm)	Travel time (minute)	Maximum amplitude (cm)
MARE	Maré	New Caledonia	167.8333	-21.5333	418	6.5	49	17.8
LENA	Lenakel	Vanuatu	169.2333	-19.5333	452	12.8	60	135.1
LIFO	Lifou	France	167.3000	-20.9000	498	16.6	68	36.6
OUIIN	Ouiné	New Caledonia	166.7000	-21.9333	515	16.5	72	27.2
NUMBO	Nouméa	New Caledonia	166.3667	-22.2333	542	1.7	107.5	4.2
THIO	Thio	New Caledonia	166.2333	-21.6000	571	8.1	80	9.8
OUIVE	Ouvéa	New Caledonia	166.5333	-20.5333	587	6.8	103	12.7
VANU	Port Vila	Vanuatu	168.2667	-17.7667	673	6.2	122	5.2
HIEN	Hienghène	New Caledonia	164.9333	-20.6667	732	4.1	101	9.5
KJNI	Norfolk Island	Australia	167.9667	-29.0667	769	11.4	88	43.6
LEVU	Lautoka	Fiji	177.4333	-17.6000	852	3.0	123	5.6
LITZ	Litzlitz	Vanuatu	167.4333	-16.1000	878	2.4	115	8.0
VITI	Suva	Fiji	178.4000	-18.1333	888	4.8	97	4.8
LUGA	Luganville	Vanuatu	167.1667	-15.5333	947	4.1	137	8.6
NCPT	North Cape	New Zealand	173.4667	-34.4333	1288	3.4	131	28.8

GBIT	Great Barrier	New Zealand	175.5000	-36.2000	1519	8.8	164	62.8
AUCT	Auckland	New Zealand	174.7667	-36.8333	1571	3.1	250	8.3
TAUT	Tauranga	New Zealand	176.1667	-37.6000	1684	1.3	189	3.9
LOTT	East Cape	New Zealand	178.1667	-37.5333	1737	6.2	164	23.9
GCSB	Gold Coast	Australia	153.4333	-27.9333	1902	20.5	240	30.5
UPOL	Apia	Samoa	188.2333	-13.8000	2026	1.4	223	4.2
CHST	Charleston	New Zealand	171.4333	-41.9000	2105	Not observable	Not observable	31.5
JACK	Jackson Bay	New Zealand	168.5667	-43.9667	2351	12.8	315	35.5
PKEM	Port Kembla	Australia	150.9333	-34.4667	2377	2.4	268	19.7
NZG	Kermadec	Kermadec	186.6000	-23.3667	1533	0.83	147	0.83
NZI	Kermadec	Kermadec	188.8000	-16.9000	1918	0.62	192.5	0.65
NZE	Hikurangi	Hikurangi	182.3000	-36.0333	1781	0.79	151.8	0.86
NZC	Hikurangi	Hikurangi	180.2000	-38.2000	1881	1.05	168.5	1.38

179

180 2.2. Bathymetric data and modelling grids

181 A nested grid configuration can be implemented in tsunami simulations to balance
182 computational efficiency and numerical accuracy. There are two nested grid configurations
183 used in this study. One is to simulate the synthetic waveforms for the inversion Green's
184 functions, and the other one is used to calculate the tsunami threat levels in New Zealand.

185 For the synthetic tsunami waveforms simulation, we made a largest modelling domain that
186 covers the nations in the South West Pacific Ocean around the earthquake source location with
187 a grid size of 120 arc-sec. A set of nested modelling domains were made to focus on each of
188 the coastal gauge with grid sizes of 40, 13.333, and 4.444 arc-sec. A combination of available
189 bathymetric data with different coverage and grid size were used for the tsunami simulation.
190 The highest resolution bathymetric data is always used to make each tsunami modelling grid.
191 The GEBCO14 gridded bathymetric data with grid size of 30 arc-sec was used and resampled
192 for the largest modelling domain and smaller domains in Australia and Fiji. A bathymetric grid
193 with resolution of 100 m is available for the area around New Caledonia and Vanuatu. Higher
194 resolution and quality bathymetric grids with resolution of 25 m are also available for the areas
195 around coastal gauges in Maré (station code: MARE), Lifou (LIFO), Ouinné (OUIN), Thio

196 (THIO), Hienghène (HIEN), Lenakel (LENA), and Port Vila (VANU). For modeling grids
197 around New Zealand coastal gauges (AUCT, CHPT, GBIT, JACK, LOTT, MNKT, NCPT, and
198 TAUT), a high quality gridded bathymetric data with grid size of 10 arc-sec is available. The
199 complete coastal gauge information can be seen in Table 1.

200 For tsunami threat level map creation, a nested grid configuration with four modelling
201 domains was prepared. The largest modelling domain covers the whole Pacific Ocean with a
202 grid size of 4 arc-min. As the main purpose of this grid setup is for tsunami threat estimate in
203 New Zealand, other locations outside the country are only simulated using the coarsest
204 modelling grid. The next grid level of modelling domain covers the entire of New Zealand and
205 have grid sizes of 1 arc-min. The last grid level with finest grid size of 15 arc-seconds includes
206 two modelling domains that cover the two New Zealand's main islands and the Chatham
207 Islands.

208

209 **3. Tsunami waveform inversion**

210 *3.1. Tsunami inversion method*

211 We first calculated two tsunami simulations using single fault models with fault
212 parameters from the GCMT and USGS W-phase MT solutions. The simulated tsunami
213 waveforms of these models are comparable. The trench is curved around the source area with
214 strike angles varying from 260° to 300° based on the USGS SLAB2.0 model (Hayes et al.,
215 2018). The trench-parallel strike angles according to USGS, GCMT and Geoscience Australia
216 are 246°, 279°, and 284° respectively. Because the strike angle from GCMT is at the middle of
217 these values, the strike of 279°, dip of 23°, and rake of 101° from the solution were assumed
218 for the fault parameters in the inversion as the strike angle from the solution is at the middle of
219 the other strike angle values (Figure 1). A fault with total length of 120 km and width of 60 km

220 was subdivided into 6 sub-faults along strike and 3 sub-faults down dip, resulting in a sub-fault
221 size of 20 km by 20 km. The top edge of the shallowest sub-faults is located along the trench
222 at depth of 1 km.

223 The seafloor displacement from each sub-fault was calculated using the Okada's formula
224 (1985). These seafloor displacement models were used as the initial modelling conditions to
225 simulate the tsunami waveforms. The linear long wave was simulated by solving the non-
226 dispersive linear shallow water equations with a finite difference method and a staggered leap-
227 frog scheme (Satake, 1995). Then a phase correction method (Watada et al., 2014; Gusman et
228 al., 2015) was applied to the simulated linear long wave to include the dispersion effects due
229 to the elasticity of the earth, seawater compressibility, and the gravitational potential variation.
230 A unit slip amount of 1 m was used to construct the tsunami Green's functions. The tsunami
231 amplitudes at some of the coastal gauges located near-field or far-field are about an order of
232 magnitude larger than the amplitudes at DART buoys. To treat the coastal and deep ocean
233 tsunami waveforms equally, we weight the DART data by 50. As fault slip must be smooth in
234 some degree (Yabuki and Matsu'ura, 1992), a spatial smoothness constraint was incorporated
235 by including a smoothing matrix consisting of a Laplacian operator. The Akaike's Bayesian
236 Information Criterion (Akaike, 1980) was used to determine the optimal value of the smoothing
237 factor. More details for the tsunami waveform inversion algorithm used in this study, which is
238 based on the non-negative least square method (Lawson and Hanson, 1995) are available in
239 previous studies (i.e., Gusman et al., 2010; Gusman et al., 2015).

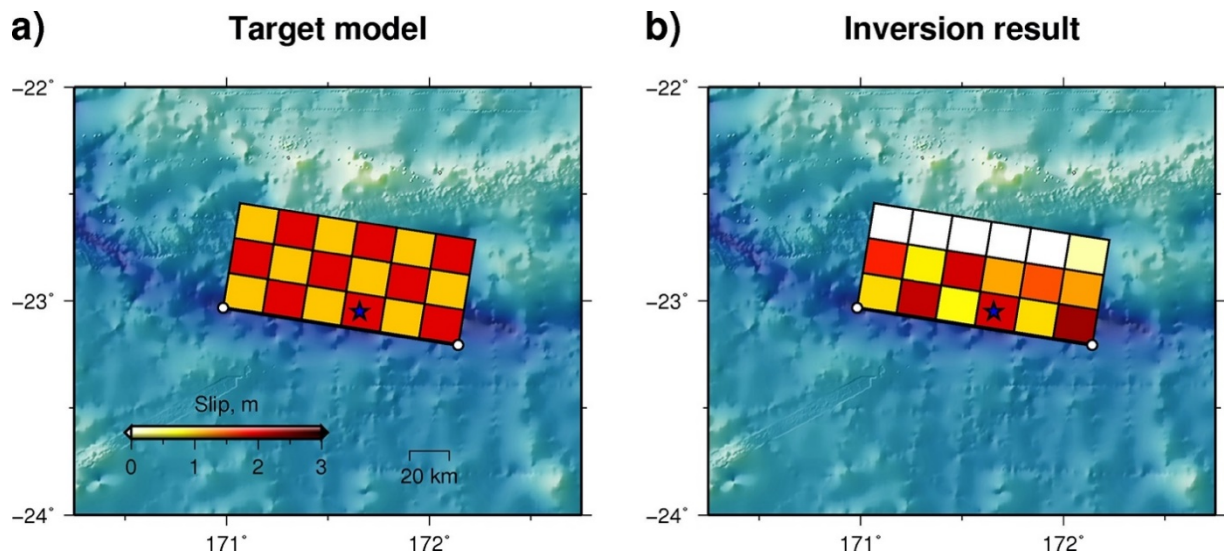
240 *3.2. Fault model resolution and quality*

241 The The earthquake source area is surrounded by coastal gauges and DART buoys. To
242 evaluate the source model resolution, we applied a checkerboard test (e.g., Lorito et al., 2010;
243 Heidarzadeh and Gusman, 2021). The checkerboard pattern for the target model was made
244 using slip amounts of 2 and 1 m (Figure 3). The target tsunami waveforms at the coastal gauges

245 and DART stations produced using this source model were degraded by adding Gaussian noise.
246 We applied the tsunami inversion code with the target waveforms to get a slip distribution. We
247 find that the checkerboard pattern on the shallower part of the fault can be well reproduced by
248 the inversion, but not the pattern on the deepest part (Figure 3). This is because there is no
249 nearby station located in the main path of the tsunami energy immediately north of the source.

250 To measure the uncertainty of the estimated slip distribution caused by various errors
251 associated with tsunami modelling, we ran 30 tsunami waveform inversions with different
252 randomly selected tsunami waveform sets at 20 out of 28 stations. The uncertainty of the
253 estimated slip distribution is represented by the standard deviation of these 30 slip distributions.

254



255

256 *Figure 3 Checkerboard test result. a) Target slip distribution. b) Slip distribution obtained by an*
257 *inversion using synthetic waveforms at the coastal gauges and DART stations generated from the target*
258 *slip model. Slip amounts of 2 and 1 m were used to make the checkerboard pattern for the target slip*
259 *model. The blue star represents the 2021 Loyalty Island earthquake epicentre.*

260

261

262 3.3. *The estimated slip distribution*

263 An initial slip distribution estimated using only tsunami waveforms recorded at the coastal
264 gauges is not so reliable as it has relatively large slip errors. It is sometime difficult to
265 accurately simulate the tsunami amplitude and arrival time at coastal gauges especially without
266 accurate bathymetric data. Some of the coastal gauges in Vanuatu, New Caledonia, and Fiji are
267 located inside a bay or lagoon showing complex bathymetric features potentially leading to
268 arrival time shifts, like shown for New Caledonia and Vanuatu by Roger et al. (2021). This
269 problem of random arrival time shifts, which may be caused by instrumental clock problems,
270 inaccurate station positions, bay effects, harbour effects, or unknown instrument responses, can
271 be solved by applying optimum waveform time shifts in the inversion as demonstrated in
272 previous studies (Romano et al., 2016; Ho et al., 2021).

273 Tsunami waveforms at DART stations can be used to help solve the problem of inaccurate
274 simulated tsunami arrival time at coastal gauges. DART stations are located at the deep ocean
275 thus accurate tsunami amplitude and arrival time can be simulated using the available global
276 bathymetric dataset. We ran an inversion to get a slip distribution using only tsunami
277 waveforms at the DART buoys. The simulated tsunami arrival times from this estimated slip
278 distribution were then assumed to be very close to the actual ones. Thus, any arrival time delay
279 could be attributed to factors other than the source location, and the simulated waveforms at
280 the coastal gauges can be used as a reference for the time shift. We found the optimum tsunami
281 time shift that minimized the waveform misfit at every coastal gauge manually. The time shift
282 applied to the simulated waveforms at the coastal gauges were up to 5.5 minutes. The tsunami
283 waveforms at these stations were shifted: MARE (3 min), OUIIN (2.58 min), THIO (4.75 min),
284 VANU (5.5 min), HIEN (3 min), NCPT (3 min), TAUT (4.6 min), and PKEM (3 min). The
285 final slip distribution was obtained from tsunami waveforms at both coastal gauge and DART

286 stations with the optimum time shift applied to the coastal gauges based upon the simulated
287 waveforms.

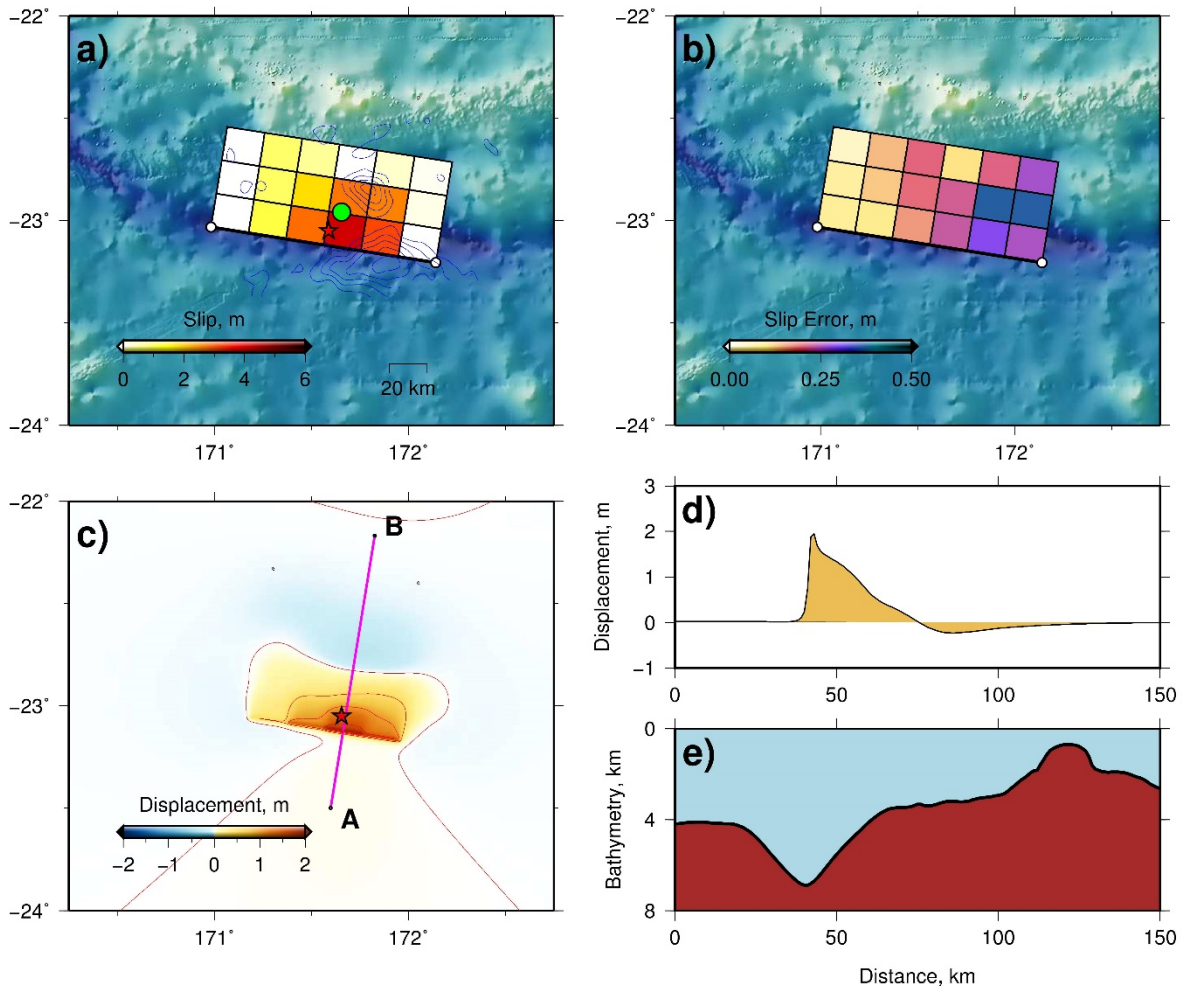
288 The estimated slip distribution has a major slip region near the trench (Figure 4a). This is
289 consistent with the result from the USGS finite fault model (USGS, 2021) (Figure 4a). The
290 maximum slip amount estimated in this study is 4.1 m (Figure 4a and Table 2). The estimated
291 maximum uplift near the trench is 2.1 m while the subsidence is 0.24 m (Figure 4c and Figure
292 4d). The calculated seismic moment from the slip distribution, assuming a rigidity of 40 GPa
293 (e.g., Fujii and Satake, 2008), is 3.39×10^{20} Nm or equal to Mw 7.65. This estimated seismic
294 moment is close to the value (4.01×10^{20} Nm) from the GCMT solution. An inversion using
295 only DART data which are relatively far away from the source gives a slightly smaller
296 calculated seismic moment (3.05×10^{20} Nm). The use of data at near-field coastal gauge
297 stations brings the estimated moment closer to the one from GCMT. Figure 5 shows that the
298 estimated slip distribution results in tsunami waveforms that largely reproduce the observations
299 at the coastal gauge and DART stations.

300 The uncertainty or error for the estimated slip distribution was calculated from the 30
301 inversions that were made with random combinations of stations. For the sub-fault with the
302 largest slip (4.1 m), the error of the estimate is ± 0.2 m or about 6% of the slip amount, which
303 is very low. Higher error percentages for the sub-faults exist mainly on the eastern part of the
304 fault model. The error distribution can be seen in Table 2 and Figure 4b. Overall, the reliability
305 of the estimated major slip region is high with very low slip errors. This error estimate and
306 also the checkerboard test result (Figure 3) show that the inversion result in the major slip region
307 is well constrained and resolved by the station coverage.

308

309

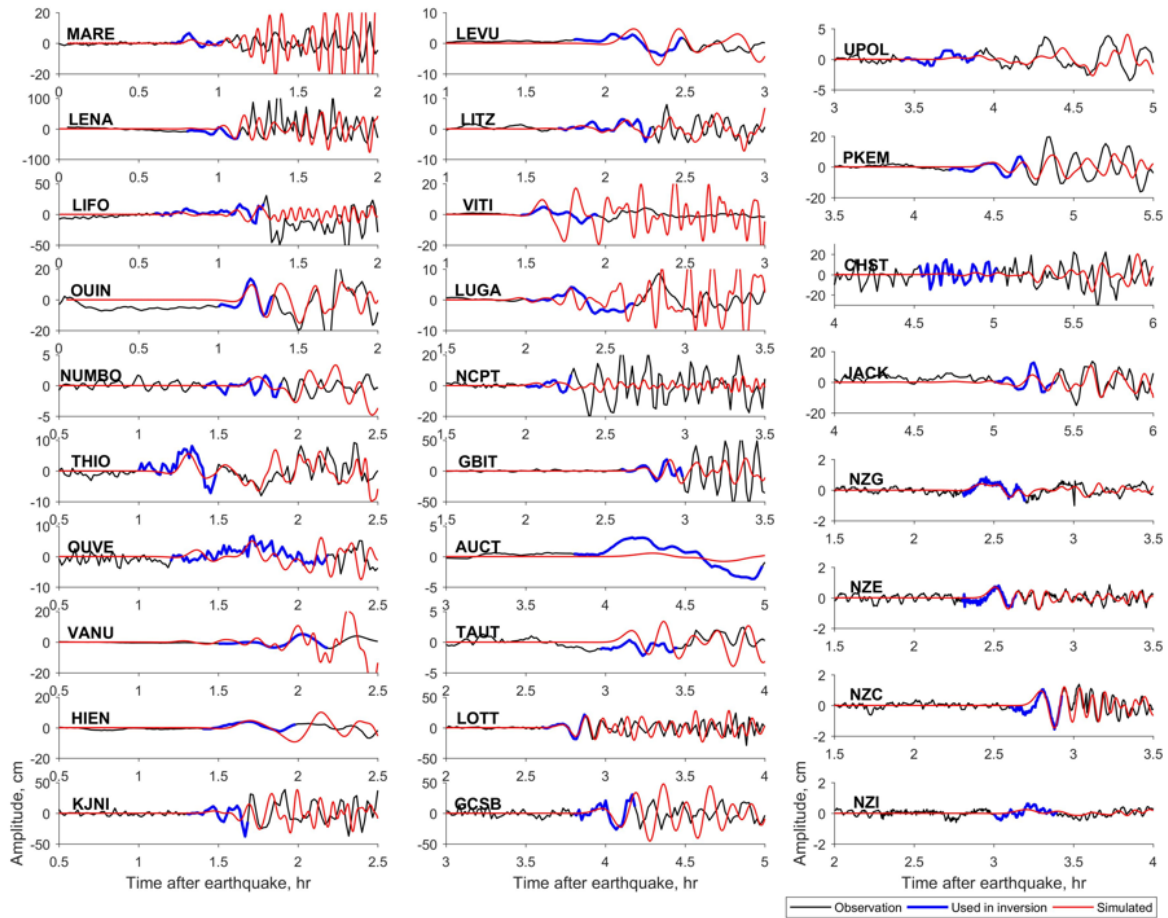
310



312

313 *Figure 4 a) Slip distribution for the 2021 Loyalty Island earthquake estimated by tsunami waveform*
 314 *inversion using tsunami waveforms recorded at coastal gauges and DART stations. Blue lines represent*
 315 *the USGS finite fault model contours at 1 m intervals, the red star represents the epicentre and the*
 316 *green circle represents the GCMT centroid location. b) Slip error map for the estimated slip distribution.*
 317 *c) Calculated co-seismic seafloor vertical displacement from the estimated slip distribution. The*
 318 *vertical displacement contour interval is 0.5 m. The purple line indicates cross-section A-B. d) The*
 319 *estimated co-seismic seafloor vertical displacement profile along cross-section A-B. e) Bathymetric*
 320 *profile along cross-section A-B.*

321



322

323 *Figure 5 Comparison between the observed (black) and simulated (red) tsunami waveforms. Blue lines*
 324 *indicate the observed waveforms that were used in the inversion.*

325

326 Table 2 Fault parameters and slip amounts from the tsunami waveform inversion

Lon (deg)	Lat (deg)	Length (km)	Width (km)	Depth (km)	Strike (deg)	Dip (deg)	Rake (deg)	Slip (m)	Error (\pm m)
172.1421	-23.2072	20	20	1	279	23	101	0	0.25
171.9489	-23.1783	20	20	1	279	23	101	3.12	0.29
171.7557	-23.1494	20	20	1	279	23	101	4.14	0.23
171.5625	-23.1206	20	20	1	279	23	101	2.8	0.16
171.3694	-23.0917	20	20	1	279	23	101	1.1	0.09
171.1762	-23.0628	20	20	1	279	23	101	0	0.08
172.1702	-23.0435	20	20	8.81	279	23	101	0.14	0.37
171.977	-23.0146	20	20	8.81	279	23	101	2.6	0.37
171.7838	-22.9858	20	20	8.81	279	23	101	2.71	0.22
171.5906	-22.9569	20	20	8.81	279	23	101	1.79	0.19
171.3974	-22.9281	20	20	8.81	279	23	101	0.92	0.13
171.2043	-22.8992	20	20	8.81	279	23	101	0	0.08
172.1983	-22.8799	20	20	16.63	279	23	101	0.09	0.26
172.0051	-22.851	20	20	16.63	279	23	101	0.31	0.21

171.8119	-22.8221	20	20	16.63	279	23	101	0.01	0.11
171.6187	-22.7933	20	20	16.63	279	23	101	0.61	0.2
171.4255	-22.7644	20	20	16.63	279	23	101	0.88	0.14
171.2323	-22.7355	20	20	16.63	279	23	101	0	0.05

327

328

329

330 **4. Tsunami Forecasting for New Zealand**

331 The COMCOT (Cornell Multi-Grid Coupled Tsunami model) program (Liu et al. 1998;
332 Wang 2006; Wang and Power 2011) was used to make the database of tsunami threat level
333 maps for New Zealand. The computer program was used to simulate tsunami generation and
334 propagation from their sources to New Zealand coasts. A simulation time of 30 hours of
335 tsunami propagation was used to ensure that maximum tsunami amplitudes were obtained. The
336 nonlinear shallow water equations were solved to simulate the tsunami. Vertical wall
337 boundaries were implemented by assuming any grid cell with an elevation larger or equal to -
338 10 cm to be land.

339 The New Zealand coast is divided into 43 tsunami warning regions (NEMA 2020). There
340 are six levels of tsunami threat in New Zealand, which are based on the coastal tsunami
341 amplitude (Table 3). However, for tsunami warning dissemination, the threat levels are also
342 grouped into three categories (Table 3), which are No Threat, Beach and Marine Threat, and
343 Land and Marine Threat. For each earthquake scenario, the 99th percentile of all coastal tsunami
344 amplitudes within each warning region is calculated and then used to identify the tsunami threat
345 level. The value for the 99th percentile is used instead of the maximum value to avoid outliers.

346

347

348

349 Table 3 Tsunami threat levels in New Zealand with their tsunami height thresholds, colour codes, descriptions
 350 and threat level names for dissemination.
 351

Threat Level	Tsunami Amplitude	Colour	Description	Threat level for dissemination
0	$h \leq 0.3$ m	White	No threat	No threat
1	$0.3 < h \leq 1$ m	Green	Threat to beach and small boats	Beach and Marine threat
2	$1 < h \leq 3$ m	Light blue	Some land threat	Land and Marine threat
3	$3 < h \leq 5$ m	Blue	Moderate land threat	
4	$5 < h \leq 8$ m	Pink	High land threat	
5	$h > 8$ m	Purple	Severe land threat	

352

353

354 *4.1. Tsunami threat levels from the estimated fault slip distribution*

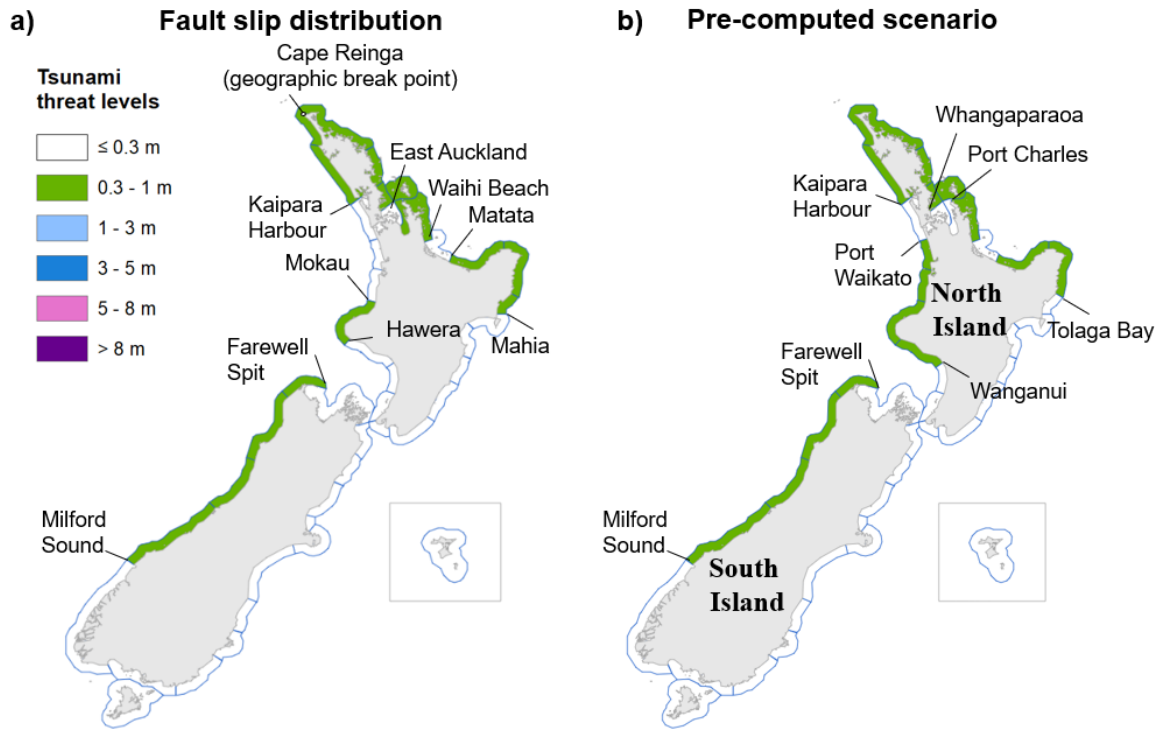
355 The tsunami simulation from the estimated fault slip distribution categorizes many
 356 tsunami warning regions as being under Beach and Marine Threat, and no region is under
 357 the Land and Marine Threat. The warning regions that should be under the Beach and
 358 Marine Threat according to that source include the West Coast of the North Island from
 359 Cape Reinga to Kaipara Harbour, and from Mokau to Hawera; the East Coast of the North
 360 Island from Cape Reinga to Waihi Beach excluding the East Coast of Auckland, and from
 361 Matata to Mahia; and the West Coast of the South Island from Farewell Spit to Milford
 362 Sound (Figure 6a). The other coastal regions are under No Threat. However, it should be
 363 noted that the procedure described here for determining the tsunami threat levels from an
 364 estimated source model is challenging during an event. The complexity of tsunami
 365 waveform inversion and the many hours required for simulating the tsunami on high
 366 resolution grids using the source model are the main drawbacks. Real-time
 367 operationalisation of an inversion-based forecasting approach can be improved with
 368 simplification of the problem including possibilities of more coarsely defining the finite
 369 fault earthquake model and using empirical coastal amplitude equations to approximate

370 coastal threat zones. In this study, the threat level map from the estimated source model is
371 used purely as reference to evaluate the forecast based on the pre-computed scenarios.
372 During the response, the New Zealand Tsunami Expert Panel (NZTEP) used a coarse
373 simplification to adjust forecasts, described further in section 5.3.

374 The amplitude of the first observed tsunami wave cycle can be much smaller than the
375 maximum observed tsunami amplitude at coastal gauges. As an example, the amplitude of
376 the first wave at NCPT (North Cape) station is only 4 cm while the maximum amplitude
377 recorded by the same station is 29 cm. The complete list of the observed first wave cycle
378 amplitudes and the maximum amplitudes at the stations can be seen in Table 1. This
379 emphasises that the simulation time should be set long enough to capture the maximum
380 simulated tsunami amplitude.

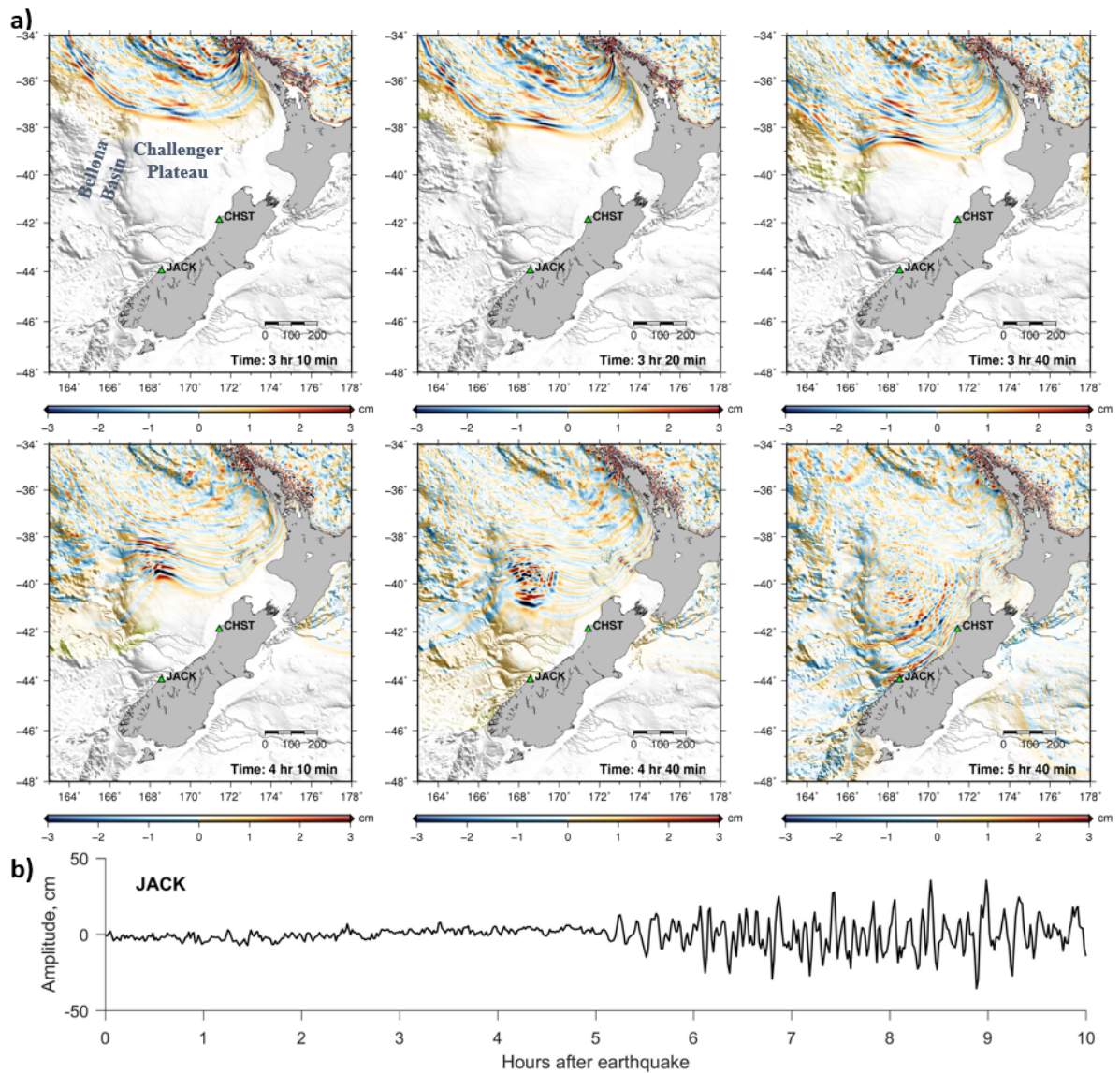
381 Several coastal zones in the South Island are identified by this method as being under
382 the Beach and Marine Threat with tsunami larger than 0.3 m. The observed first tsunami
383 wave cycle amplitude in Jackson Bay which is located in the West Coast region of South
384 Island is 13 cm, while the maximum amplitude is 35 cm which validates the tsunami threat
385 level from the estimated fault slip distribution. Both simulation and observation at Jackson
386 Bay show that the tsunami is even higher than in some of the stations in the North Island.
387 Bathymetric features, and especially the Challenger Plateau and Bellona Basin (Figure 7b)
388 (Uruski, 2010), allow the tsunami to focus part of its energy on the West Coast of the South
389 Island as shown by the snapshots of the tsunami propagation shown in Figure 7a and the
390 maximum tsunami amplitude distribution in Figure 7c. The part of the tsunami propagating
391 over the deeper Bellona Basin goes with a faster speed than the part propagating over the
392 neighbouring shallower Challenger Plateau: the tsunami front slows down when arriving
393 on the northwesternmost part of the Challenger Plateau, wrapping around the set of
394 seamounts in the area around 38°S, 167°E (Rowden et al., 2005) and concentrating the

395 energy at the back of the seamounts, with a trajectory still oriented toward the West Coast
 396 of the South Island but with higher amplitudes. In addition, numerous submarine canyon
 397 complexes located along the southwestern margin of the Challenger Plateau (Neil et al.,
 398 2015) act as waveguides to focus tsunami waves on specific locations and can also explain
 399 the higher waves recorded at Jackson Bay (Figure 7d).



400
 401 *Figure 6 Tsunami threat level maps for New Zealand from a) a computation using the estimated fault*
 402 *slip distribution of the 2021 Loyalty Island earthquake and b) a pre-computed earthquake scenario*
 403 *(Mw 7.7) that best matches the epicentre and magnitude of the earthquake.*

404
 405



406

407

408

409 *Figure 7 a) Simulated tsunami propagation snapshots from the 2021 Loyalty Island earthquake source model over Bellona*
 410 *Basin and Challenger Plateau near New Zealand. Green triangles indicate the locations of JACK and CHST coastal gauges. b)*
 411 *Observed tsunami waveforms at JACK (Jackson Bay) coastal gauge.*

412

413 *4.2. Tsunami threat levels from a nearest pre-computed scenario*

414 Earthquake scenarios in subduction zones around the Pacific Ocean were used to build
 415 a database of tsunami threat level in New Zealand. The size of the fault patches used for
 416 the earthquake scenarios in the New Hebrides subduction zone is 50 km long and 25 km

417 wide. The earthquake scenario moment magnitudes (M_w) are ranged from 6.9 to 9.3, with
418 magnitude interval of 0.2. The distance between the scenario's epicentres for magnitudes
419 7.5, 7.7, and 7.9 is 150 km. The assumed fault parameters and orientations for the fault
420 models in this region are based on fault patches developed by the U.S. National Oceanic
421 and Atmospheric Administration (NOAA) (Gica et al., 2008) and those available from
422 Power et al. (2012). An earthquake scenario in the New Hebrides subduction zone with a
423 moment magnitude of 7.7 that is the nearest to the 2021 Loyalty Island earthquake epicentre
424 was selected from the database. This scenario epicentre is ~ 70 km westward the actual
425 epicentre. The uniform slip earthquake scenario has four fault patches and a slip amount of
426 2.2 m.

427 The predicted threat levels at most of the coastal regions (38 out of 43 regions) matched
428 the reference ones (Figure 6). Just like the threat level map from the fault slip distribution,
429 the one from the pre-computed scenario has no warning region that should be under the
430 Land and Marine Threat (Figure 6b). The warning regions that should be under the Beach
431 and Marine Threat include the West Coast of the North Island from Cape Reinga to Kaipara
432 Harbour, and from Port Waikato to Wanganui; the East Coast of the North Island from
433 Cape Reinga to Waihi Beach excluding the region from Whangaparaoa to Port Charles,
434 and from Matata to Tolaga Bay (Figure 6b). While the threat levels for the warning regions
435 in the South Island from the two models are the same. The selected scenario underestimated
436 the tsunami threat in two warning regions by one level lower and overestimated the threat
437 in three warning regions by one level higher.

438

439 *4.3. Interpolated tsunami threat levels from pre-computed scenarios*

440 The tsunami from the earthquake can be approximated by interpolating simulation
441 results from scenarios located around the epicentre (e.g., Tatehata, 1998). Here we

442 interpolated the threat level maps from these two scenarios with the inverse distance
 443 weighting method (Shepard, 1968). A general way of finding an interpolated tsunami threat
 444 level (f_i) in the 43 warning regions ($i = 1, 2, \dots, 43$) for a given epicentre based on pre-
 445 computed tsunami threat level in the database $f_{i,j}$ for $j = 1, 2, \dots, N_s$ is to use the following
 446 equation:

$$447 \quad f_i = \begin{cases} \frac{\sum_{j=1}^{N_s} w_j \cdot f_{i,j}}{\sum_{j=1}^{N_s} w_j}, & \text{if } d \neq 0 \text{ for all } j, \\ f_{i,j}, & \text{if } d = 0 \text{ for some } j, \end{cases}$$

448 Eq. (1)

449
 450 where

$$451 \quad w_j = \frac{1}{d^p}$$

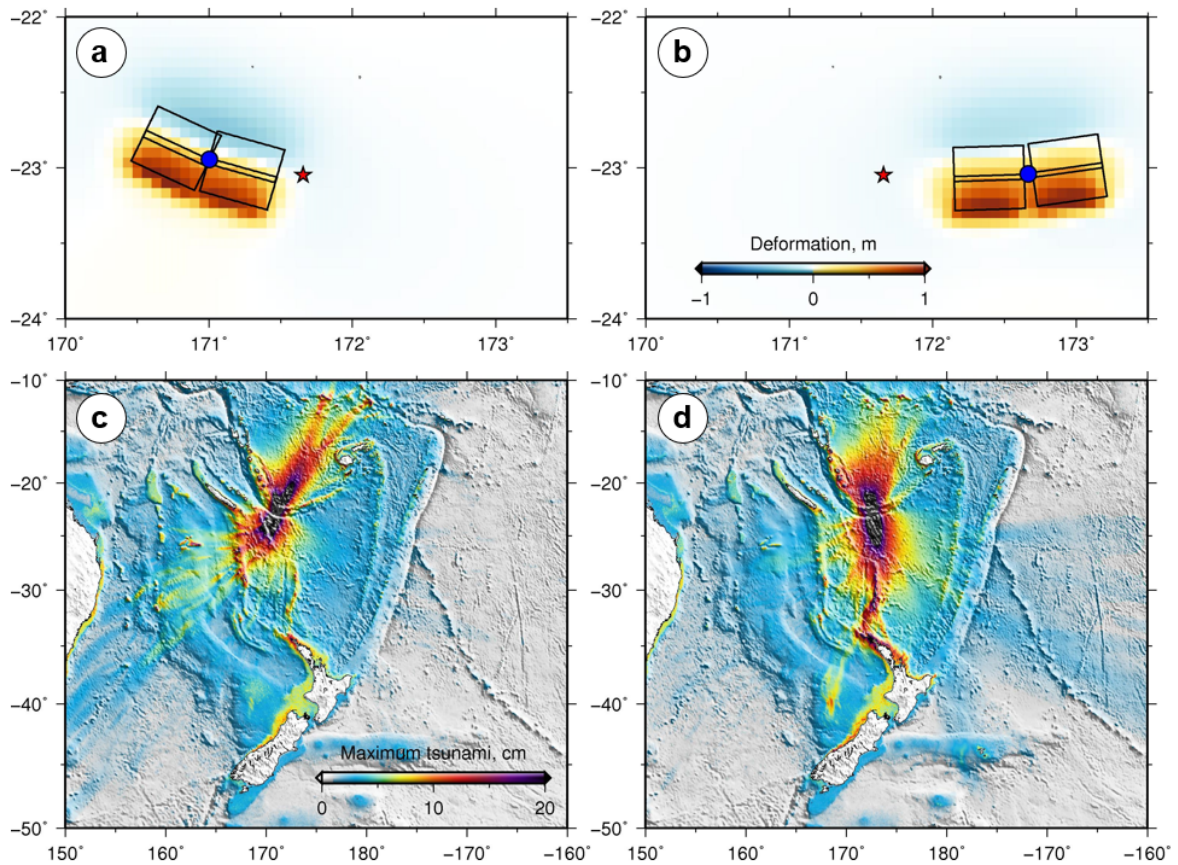
452 Eq. (2)

453
 454 , d being the distance between the earthquake epicentre and scenario epicentre (reference
 455 point), N_s the number of scenarios which is 2 in this case, and p the power parameter set
 456 to 1.

457 As mentioned above, the reference point or epicentre of the selected scenario is
 458 westward the actual epicentre. We produced a threat level map by interpolating the tsunami
 459 heights in the warning zones from the selected nearest scenario with Mw7.7 located west
 460 of the epicentre (West Mw7.7 described in 4.2) and the second nearest scenario with also
 461 Mw7.7 located east of the epicentre (East Mw7.7). The vertical displacements and
 462 maximum tsunami amplitude distributions from these two scenarios can be seen in Figure
 463 8. The interpolation result shows that there is one warning region which is the North Cape
 464 area from Ahipara to Bay of Islands (Figure 9a) that should be under the Land and Marine

465 Threat, while there is no region under this threat category from the previous two models.
466 The warning region from Waihi beach to Matata should be under No Threat according to
467 the reference map (Figure 6a), which is a level lower than the one according to the
468 interpolation result (Figure 9a). While the threat levels for the other warning regions are the
469 same as those in the selected scenario.

470 The interpolated threat levels (Figure 9a) at most of the coastal regions (36 out of 43
471 regions) matched the reference ones (Figure 6a). Based on the reference threat level map,
472 the selected scenario underestimated the tsunami threat in two warning regions by one level
473 lower and overestimated the threat in five warning regions by one level higher. This makes
474 the forecast accuracy from the interpolation result slightly worse than the one from the
475 selected scenario nearest to the epicentre. The interpolated threat levels are overall slightly
476 higher than the one from the selected nearest scenario. The overestimated warning levels
477 are because the earthquake source model that was used for to make the reference map has
478 a slightly smaller seismic moment ($M_0 = 3.39 \times 10^{20}$ Nm equivalent to moment magnitude
479 Mw7.65) than the pre-computed scenario one (Mw7.7).

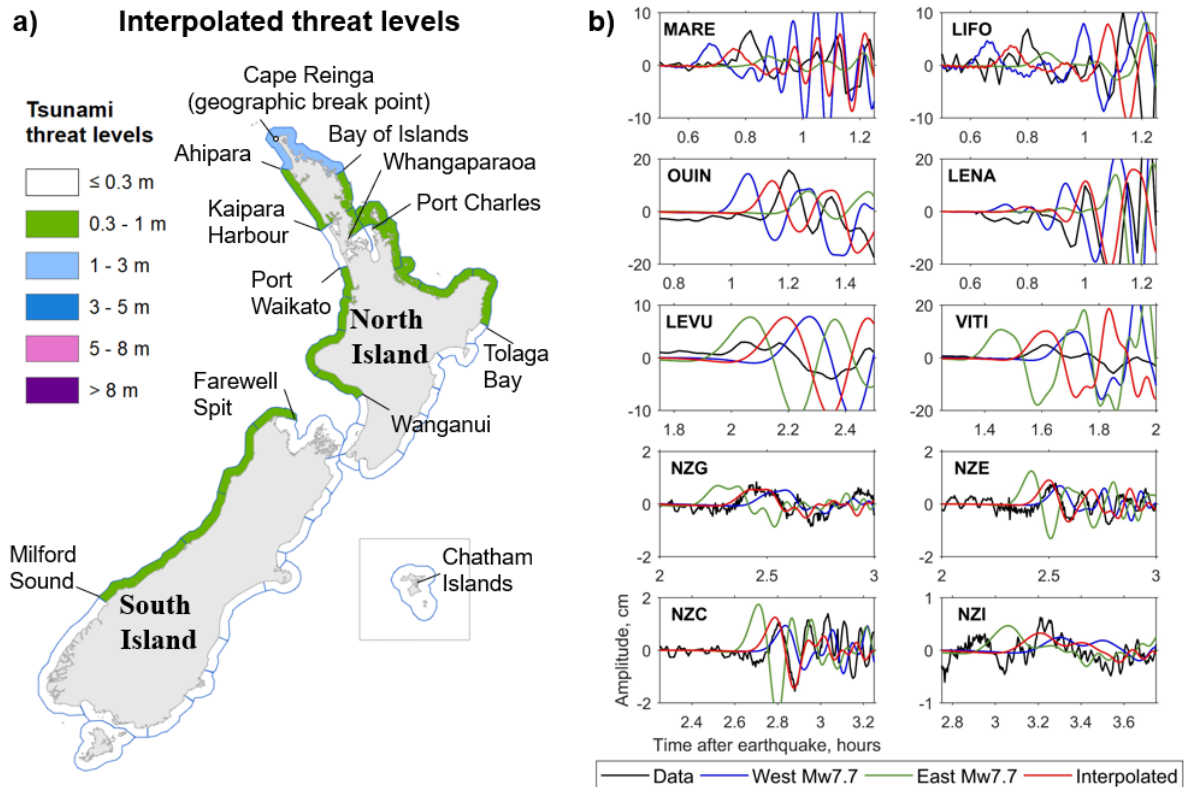


480

481 *Figure 8. Initial tsunami simulation of seafloor displacements and simulated tsunami amplitude distributions for the (a and*
 482 *(c) WestMw7.7 uniform slip scenario (nearest scenario) and (b and d) EastMw7.7 uniform slip scenario. Black rectangles*
 483 *indicate the fault patches used by the scenario. The blue star represents the earthquake epicentre, while the blue dot*
 484 *represents the reference point/epicentre for the scenario.*

485

486



487

488 *Figure 9 a) Threat level map obtained by interpolating the results from two Mw7.7 scenarios nearest to the epicentre. b)*
 489 *Observed, simulated and interpolated tsunami waveforms. Red lines indicate the interpolated tsunami waveforms from*
 490 *tsunami waveforms of the selected nearest scenario Mw7.7 located west of the epicentre (blue lines) and those of a second*
 491 *nearest scenario Mw7.7 located east of the epicentre (green lines). The locations of the scenarios are shown in Figure 8a*
 492 *and b.*

493

494 5. Discussion

495 5.1. Toward improved real-time update of tsunami threat level maps

496 The tsunami forecast using pre-computed scenario database approach may not be
 497 enough if it only relies on the earthquake magnitude estimate. Tsunami records at coastal
 498 gauges and DART stations can be used to confirm or update the tsunami threat level. For
 499 this event, the tsunami arrived in the North Cape of New Zealand approximately 2 hours
 500 after the earthquake. Within 1.5 hours after the earthquake, at least one complete tsunami
 501 wave cycle had been recorded at four coastal gauges (MARE, OUIN, LIFO, and LENA)
 502 located in the azimuthal quadrant west-northwest of the epicentre. The sea level recorded

503 within 2 hours after the earthquake at LEVU and VITI which are located in Fiji to the east
504 of the epicentre can be used to evaluate the tsunami. While the tsunami arrival times at the
505 two closest DART stations (NZG and NZE) are approximately 2.5 hours after the
506 earthquake. We note that planned network expansion will provide 3 additional DART
507 stations within one-hour travel time of this earthquake source. When complete, the array is
508 designed to detect events originating from any Hikurangi/Kermadec/Tonga/New Hebrides
509 trench source within 30 minutes. Any warning update for this event based on the currently
510 operational DART stations would be too late for first wave arrival at North Cape but could
511 be valuable prior to maximum wave arrivals and also for dynamic forecasting during the
512 latter stages of the threat, supporting staggered de-escalation. This shows that the already
513 planned additional DART stations (Power et al., 2018) need to be deployed around the New
514 Hebrides subduction zone to enable a rapid characterization of any tsunami generated in
515 this area that threaten New Zealand and the nearby islands.

516 The existing pre-computed tsunami waveforms at coastal gauges outside New Zealand
517 were simulated using a low-resolution modelling grid (4 arc-min) as explained in Section
518 2.2. To make the observed tsunami waveform at coastal gauges more useful in validating
519 or updating a tsunami warning, the pre-computed tsunami waveforms need to be obtained
520 using high resolution grids. In this study we simulated the tsunamis at coastal gauges with
521 our highest modelling grid resolution for the two uniform slip scenarios (West Mw 7.7 and
522 East Mw 7.7) located around the actual epicentre (Figure 8a and b).

523 The tsunami waveforms from these two scenarios can be interpolated to get the
524 estimated tsunami waveforms for the event (Figure 9b). We used a waveform interpolation
525 method (Wang et al., 2019) which is based on the Huygens-Fresnel principle. Equations
526 Eq. (1) and Eq. (2) can be modified and then used to interpolate the tsunami arrival times
527 and amplitudes for an interpolated event. First, we estimated the arrival time at the stations

528 for the interpolated event. The interpolated arrival time at k^{th} station of t_k^{arr} is calculated
 529 from the simulated arrival time from the scenarios $t_{k,j}^{\text{arr}}$ using the following equation:

$$530 \quad t_k^{\text{arr}} = \frac{\sum_{j=1}^{N_s} w_j \cdot t_{k,j}^{\text{arr}}}{\sum_{j=1}^{N_s} w_j}$$

531 *Eq. (3)*

532 The simulated arrival time of each scenario is marked when the amplitude of the simulated
 533 tsunami at the station reached a threshold. The thresholds for coastal gauges are >1 cm
 534 while that for DARTs is 0.1 cm. Then the tsunami waveforms (y_k) can be interpolated from
 535 the amplitudes of the two simulated waveforms ($Y_{k,j}$) using the following equation:

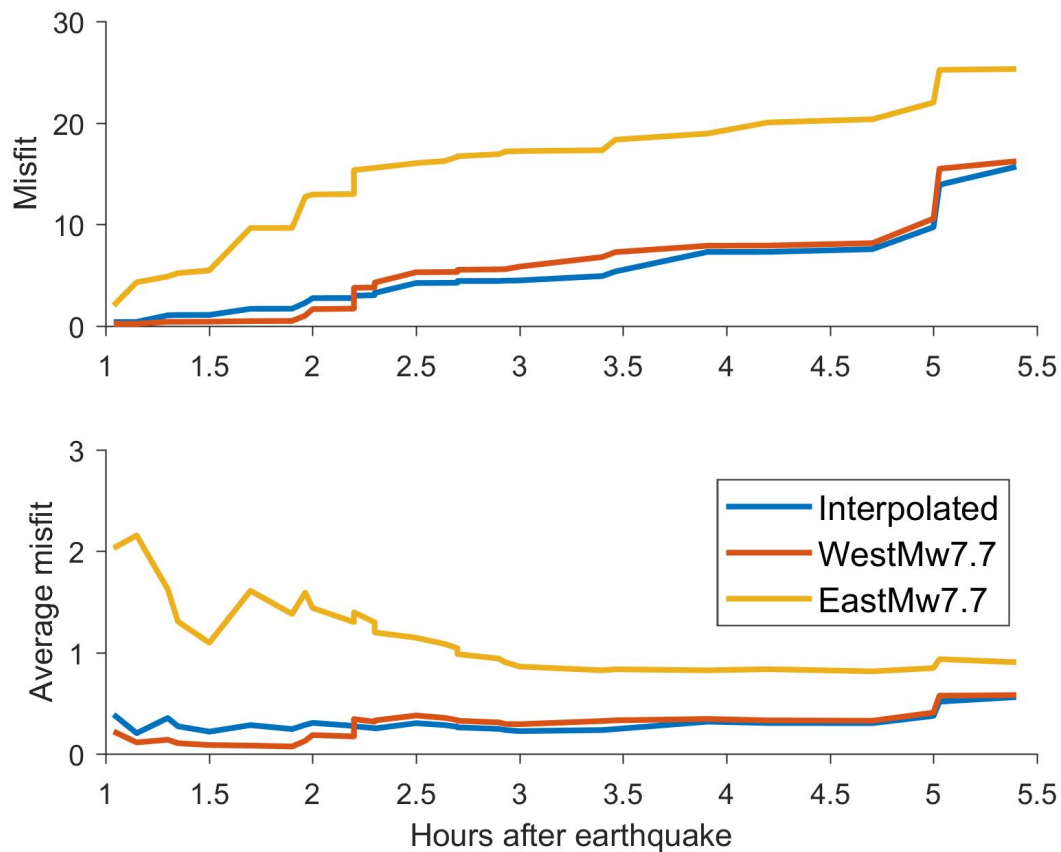
$$536 \quad y_k(t - t_k^{\text{arr}}) = \frac{\sum_{j=1}^{N_s} w_j \cdot Y_{k,j}(t - t_{k,j}^{\text{arr}})}{\sum_{j=1}^{N_s} w_j}$$

537 *Eq. (4)*

538 The interpolated tsunami waveforms fit better the observations in term of both
 539 amplitude and arrival time compared to those from the two nearest Mw7.7 scenarios as
 540 shown in Figure 9b. At coastal gauges located west of the epicentre such as MARE, LIFO,
 541 OUIIN and LENA, the West Mw7.7 scenario tsunami arrived earlier than the observation,
 542 and the East Mw7.7 scenario tsunami arrived after the observed arrival time. At station
 543 located east of the epicentre such as LEVU and VITI coastal gauges and the DARTs, the
 544 East Mw7.7 scenario tsunami arrived earlier than the observation, and the West Mw7.7
 545 scenario tsunami arrived after the observed arrival time. While the interpolated waveforms
 546 arrived almost at the same time as the observations. To evaluate the scenarios the tsunami
 547 waveforms misfits are calculated. The data-simulation misfit is defined
 548 as $\sum \frac{|\max(d) - \max(s)|^2}{|\max(d)| |\max(s)|}$, where d and s are the peak amplitudes of the first wave cycle of the
 549 observed and simulated tsunami waveforms, respectively. The amplitude data-simulation
 550 misfit for the interpolated (misfit = 15.7) and WestMw7.7 (misfit = 16.2) tsunami

551 waveforms are very similar, and these values are much smaller than 25.3 from EastMw7.7
552 scenario (Figure 10). Some selected waveforms used to calculate these misfits can be seen
553 in Figure 9b.

554 In retrospect, after the earthquake moment magnitude became available, we had two
555 tsunami threat level maps. One was from the scenario nearest to the epicentre and the other
556 was an interpolated threat level map from two scenarios nearest to the epicentre. To make
557 a conservative tsunami forecast, the higher threat level at each warning zone from the two
558 scenarios should be selected. The tsunami waveforms recorded within 1.5 hours at the
559 nearby four coastal gauges showed that the interpolated scenario have tsunami waveforms
560 with better tsunami arrival time but slightly worse tsunami amplitude predictions
561 ($\text{misfit}_{1.5\text{hours}} = 1.09$) compared to those from the nearest scenario to the epicentre
562 ($\text{misfit}_{1.5\text{hours}} = 0.42$) (Figure 10). The analysis with more tsunami waveforms at DART
563 stations and coastal gauges that were available more than 2.2 hours after the earthquake
564 suggest that the best scenario was the interpolated scenario which has a smaller misfit
565 (Figure 10) and better tsunami arrival time prediction.



566

567 *Figure 10 Misfit and average misfit of tsunami amplitude at observation stations from the interpolated, WestMw7.7,*
 568 *EastMw7.7 scenarios. The misfit is increasing over time as the number of stations used for the calculation increases. The*
 569 *average misfit is the misfit divided by the number of stations.*

570

571 *5.2. Expanding the scenario database*

572 The current tsunami threat level maps for New Zealand are all based on thrust
 573 earthquake scenarios. The 2021 Loyalty Island earthquake was also a thrust event. The
 574 magnitude and focal mechanism of the earthquake can be confidently concluded in about
 575 2 hours before the tsunami reaches any New Zealand coastline or 30 minutes after the
 576 earthquake occurred. However, initial earthquake magnitude estimates for unusual kinds
 577 of tsunamigenic earthquakes such as tsunami earthquakes (Kanamori, 1972) may not be
 578 accurately obtained as quickly as those of typical thrust faulting earthquakes. Tsunami
 579 earthquake scenarios may be further developed by assuming a rigidity of 10 GPa which is
 580 smaller than the currently used one of 40 GPa when calculating the slip amount from any

581 given moment magnitude. It has been shown that the use of smaller rigidity for tsunami
582 earthquakes with a given moment magnitude provides better tsunami impact predictions
583 (Tanioka et al., 2017).

584 Large tsunamigenic intraplate earthquakes with the potential to create disastrous
585 tsunamis may also occur with normal faulting mechanisms, such as the 1933 Sanriku (Mw
586 8.4), 1977 Sumba (Mw 8.3), and 2017 Chiapas (Mw8.2) earthquakes (Lynnes and Lay,
587 1988; Tanioka and Satake, 1996; Gusman et al., 2009; Gusman et al., 2018; Melgar et al.,
588 2018). There is currently no scenario in the database with normal faulting mechanism, thus
589 an update that includes this earthquake mechanism is recommended.

590 As shown above, if the current pre-computed scenario were used to forecast the tsunami
591 in the near field, the actual tsunami arrived after the predicted arrival time in New
592 Caledonia, while the tsunami arrived before the predicted arrival time in Fiji. This is
593 because the selected scenario is Westward the actual epicentre and the distance between
594 scenarios is 150 km. Also, the plate boundary is curved around the earthquake source and
595 the strike angles of fault model patches there varies from 260° to 300°. These suggest that
596 the earthquake scenarios around the source region are not dense enough for those two
597 countries. A simple rule for the distance between the scenarios based on the earthquake
598 magnitude may be applied to expand the scenarios. The distance can be set to be at least
599 half of the typical fault length for a given earthquake magnitude. This will give scenario
600 distance of 50 km for earthquake scenarios with magnitudes from 7.5 to 7.9. Interpolation
601 between scenarios may be more effective than having more scenarios and would be
602 computationally more efficient to try to cover every possible earthquake that might occur.
603 Although adding more scenarios is preferred for areas like the Southern New Hebrides
604 subduction zone that have fault patches with a significant range (>20°) of strike angles.

605

606

5.3. Rapid Response

607

608

609

610

611

612

613

614

615

616

617

618

619

620

621

622

623

624

625

626

627

628

In real-time, the response relied on threat-level maps derived from precalculated scenarios as described above. The NZTEP used modelling based on a coarse simplification of the earthquake source to validate the pre-calculated models. These simplified models used 50 km × 100 km subduction zone unit sources and precalculated wave propagation Green's Functions from the propDB database accessed within the ComMIT software (Titov et al., 2011). One unit source (NV37b centered at 22.69° S – 171.55° E) was used to represent the earthquake rupture with homogeneous slip. Based on a seismic magnitude of Mw7.7, initial response simulations calculated the tsunami wavefield resulting from 2m slip. The resulting forecasts were used to augment the threat maps based on the pre-calculated scenarios described above. During the response, it was noted that forecast amplitudes were less than those recorded at coastal tide gauges and DARTs. To account for this discrepancy, a precautionary approach was taken and the modelled slip was adjusted to ~4m, increasing the estimated earthquake magnitude to Mw7.9. This is compatible with the maximum slip amount of 4.1 m as described above. The pragmatic effect of this adjustment was to inform the expect duration of the Marine and Beach threat. We note that manual calibration of the forecast is an interim step toward real-time inversion based forecasting. Current and future work is aimed at implementing inversion of DART data and improved forecasting. The Loyalty Island earthquake and tsunami represent a valuable datapoint to help characterize the uncertainties involved in coarse discretization of the earthquake source and determine an acceptable tradeoff between computational time and forecast accuracy.

629 **6. Conclusions**

630 We estimated the slip distribution of the 2021 Loyalty Islands earthquake from tsunami
631 waveforms recorded at 4 DART stations and 24 coastal gauges. The tsunami threat levels in
632 coastal regions in New Zealand from the estimated slip distribution are then used as a reference
633 map to evaluate the performance of our pre-computed earthquake scenario database selection
634 and interpolation approaches for tsunami forecasting. The main results are:

635 i) The major slip region of the estimated fault slip distribution is located near the
636 trench with maximum slip amount of 4.1 m. The computed seismic moment for the
637 source model of 3.39×10^{20} Nm (Mw7.65) is consistent with the Global Centroid
638 Moment Tensor and USGS W-phase Moment Tensor solutions.

639 ii) The coastal gauge records clearly showed that the largest amplitudes may be
640 observed many hours after the tsunami arrived and the oscillation may last for more
641 than 10 hours after the earthquake. Therefore, long tsunami simulation time is
642 needed to properly calculate the potential tsunami threat from an earthquake
643 scenario, for our scenarios the simulation time is 30 hours.

644 iii) The threat level of coastal regions in the West Coast of South Island of New Zealand
645 is the same as some of those in the North Island even though the two locations are
646 as far as 1000 km apart. The tsunami simulation results suggest that the tsunami
647 was refracted by the Challenger Plateau and Bellona Basin which refocused some
648 of its energy towards the West Coast of South Island.

649 iv) A tsunami threat level map can be obtained by interpolating two nearest Mw 7.7
650 earthquake scenarios (WestMw7.7 and EastMw7.7) to the epicentre available in the
651 database. In this case the tsunami waveforms recorded at the coastal gauges and
652 DART stations show that the interpolated waveforms matched the observed
653 tsunami amplitude and arrival time better than those from the two Mw 7.7 in the

654 database. However, threat level validation or update from the analysis of tsunami
655 data must be done with caution especially if the station azimuthal coverage is still
656 poor during an event. The azimuthal coverage can increase as the tsunami
657 propagates and is recorded by more stations.

658 v) The threat level maps from the nearest scenario and the interpolation both give
659 accurate tsunami forecast for most warning zones. For a conservative forecast an
660 ensemble tsunami threat level map can be obtained from the two maps. In this case
661 the ensemble tsunami forecast is the same as the interpolation result.

662 vi) The existing earthquake scenarios are not dense enough to accurately forecast the
663 tsunami in countries near the epicentre such as New Caledonia, Vanuatu and Fiji.
664 A solution for this problem is by densifying earthquake scenarios. Another option
665 with much lower computational cost is by interpolating the threat levels and tsunami
666 waveforms from the existing available scenarios.

667

668 **7. Acknowledgements**

669 We thank Maxime Duphil (IRD, Nouméa, New Caledonia) for providing us with the
670 bathymetric grid around some of the coastal gauges in New Caledonia. We thank David
671 Burbidge from GNS Science, New Zealand for reviewing our manuscript. Funding for parts of
672 this work was provided by the New Zealand Rapid Characterisation of Earthquakes and
673 Tsunami programme. DART data available on request from the authors or New Zealand's
674 GeoNet (www.geonet.org.nz). Tide gauge data available from the Intergovernmental
675 Oceanographic Commission of UNESCO (IOC) (<http://www.ioc-sealevelmonitoring.org/>).
676 Figures in the main text were made by GMT (<https://www.generic-mapping-tools.org>) and
677 MATLAB (www.mathworks.com) software.

678

679 **8. References**

680

681 Calmant S., Pelletier B., Bevis M., Taylor F., Lebellegard P., and Phillips, D. (2003). New
682 insights on the tectonics of the New Hebrides subduction zone based on GPS results, J.
683 Geophys. Res., 108, B6, 2319-2340, 2003.

684 Duphil, M., Aucan, J., Lefèvre, J., Pelletier, B., Roger, J., Thomas, B. (2021). Tsunami hazard
685 assessment in New Caledonia. TsuInfo Alert, 23(1),
686 https://www.dnr.wa.gov/publications/ger_tsuinfo_2021_v23_no1.pdf.

687 Fry, B.; Gledhill, K.R.; Benites, R.A. (2018). Ground motions in New Zealand from Kermadec
688 megathrust earthquakes. Lower Hutt, N.Z.: GNS Science. GNS Science report 2018/33. 17
689 p.; doi: 10.21420/7J43-G338

690 Fry, B.; McCurrach, S.-J.; Gledhill, K.R.; Power, W.L.; Williams, M.; Angove, M.; Arcas, D.;
691 Moore, C. (2020). Sensor network warns of stealth tsunamis. *Eos*, 101: doi:
692 10.1029/2020EO144274

693 Fujii, Y., & Satake, K. (2008). Tsunami sources of the November 2006 and January 2007 great
694 Kuril earthquakes. *Bulletin of the Seismological Society of America*, 98(3), 1559-1571.

695 Gica, Edison. "Development of the forecast propagation database for NOAA's Short-term
696 Inundation Forecast for Tsunamis (SIFT)." (2008).

697 Greenslade, D., Allen, S.C.R., Simanjuntak, M.A. (2011). An evaluation of tsunami forecasts
698 from the T2 scenario database. *Pure and Applied Geophysics*, 168, 1137-1151,
699 <https://doi.org/10.1007/s00024-010-0229-3>.

700 Gusman, A. R., Tanioka, Y., Matsumoto, H., & Iwasaki, S. I. (2009). Analysis of the Tsunami
701 Generated by the Great 1977 Sumba Earthquake that Occurred in Indonesia Analysis of the
702 Tsunami Generated by the Great 1977 Sumba Earthquake that Occurred in Indonesia.
703 *Bulletin of the Seismological Society of America*, 99(4), 2169-2179.

704 Gusman, A. R., Tanioka, Y., Kobayashi, T., Latief, H., & Pandoe, W. (2010). Slip distribution
705 of the 2007 Bengkulu earthquake inferred from tsunami waveforms and InSAR data. *Journal*
706 *of Geophysical Research: Solid Earth*, 115(B12).

707 Gusman, A. R., Tanioka, Y., MacInnes, B. T., & Tsushima, H. (2014). A methodology for
708 near- field tsunami inundation forecasting: Application to the 2011 Tohoku tsunami.
709 *Journal of Geophysical Research: Solid Earth*, 119(11), 8186-8206.

710 Gusman, A. R., Murotani, S., Satake, K., Heidarzadeh, M., Gunawan, E., Watada, S., & Schurr,
711 B. (2015). Fault slip distribution of the 2014 Iquique, Chile, earthquake estimated from
712 ocean- wide tsunami waveforms and GPS data. *Geophysical Research Letters*, 42(4), 1053-
713 1060.

714 Gusman, A. R., Mulia, I. E., & Satake, K. (2018). Optimum sea surface displacement and fault
715 slip distribution of the 2017 Tehuantepec earthquake (Mw 8.2) in Mexico estimated from
716 tsunami waveforms. *Geophysical Research Letters*, 45(2), 646-653.

717 Gusman, A.R.; Lukovic, B.; Peng, B. (2020). Tsunami threat level database update: regional
718 sources and tsunami warning text. Lower Hutt, N.Z.: GNS Science. GNS Science report
719 2019/83. 57 p.; doi: 10.21420/PTDC-NS18

720 Harig, S., Immerz, A., Weniza, Griffin, J., Weber, B., Babeyko, A., rakowsky, N., Hartanto,
721 D., Nurokhim, A., Handayani, T., Weber, R. (2019). The tsunami scenario database of the
722 Indonesia Tsunami Early Warning System (InaTEWS): evolution of the coverage and the
723 involved modeling approaches. *Pure and Applied Geophysics*, 177, 1379-1401,
724 <https://doi.org/10.1007/s00024-019-02305-1>.

725 Hayes, G. P., Moore, G. L., Portner, D. E., Hearne, M., Flamme, H., Furtney, M., & Smoczyk,
726 G. M. (2018). Slab2, a comprehensive subduction zone geometry model. *Science*,
727 362(6410), 58-61.

728 Heidarzadeh, M., & Gusman, A. R. (2021). Source modeling and spectral analysis of the Crete
729 tsunami of 2nd May 2020 along the Hellenic Subduction Zone, offshore Greece. *Earth,*
730 *Planets and Space, 73*(1), 1-16.

731 Ho, T. C., Satake, K., Watada, S., & Fujii, Y. (2019). Source estimate for the 1960 Chile
732 earthquake from joint inversion of geodetic and transoceanic tsunami data. *Journal of*
733 *Geophysical Research: Solid Earth, 124*(3), 2812-2828.

734 Hoshiba, M., & Ozaki, T. (2014). Earthquake Early Warning and Tsunami Warning of the
735 Japan Meteorological Agency, and Their Performance in the 2011 off the Pacific Coast of
736 Tohoku Earthquake Mw 9.0). In *Early warning for geological disasters* (pp. 1-28). Springer,
737 Berlin, Heidelberg.

738 Ioualalen, M., Pelletier, B., & Gordillo, G. S. (2017). Investigating the March 28th 1875 and
739 the September 20th 1920 earthquakes/tsunamis of the Southern Vanuatu arc, offshore
740 Loyalty Islands, New Caledonia. *Tectonophysics, 709*, 20-38.

741 Kanamori, H. (1972). Mechanism of tsunami earthquakes. *Physics of the earth and planetary*
742 *interiors, 6*(5), 346-359.

743 Lawson, C. L., & Hanson, R. J. (1995). Solving least squares problems. Society for Industrial
744 and Applied Mathematics.

745 Liu PLF, Woo SB, Cho YS. 1998. Computer programs for tsunami propagation and inundation.
746 New York (NY): Cornell University. Technical Report.

747 Lorito, S., Piatanesi, A., Cannelli, V., Romano, F., & Melini, D. (2010). Kinematics and source
748 zone properties of the 2004 Sumatra- Andaman earthquake and tsunami: Nonlinear joint
749 inversion of tide gauge, satellite altimetry, and GPS data. *Journal of Geophysical Research:*
750 *Solid Earth, 115*(B2).

751 Lynnes, C. S., & Lay, T. (1988). Source process of the great 1977 Sumba earthquake. *Journal*
752 *of Geophysical Research: Solid Earth, 93*(B11), 13407-13420.

753 Matias, L., Baptista, M.A., Omira, R., Annunziato, A., Franchello, G., Carrilho, F. (2012).
754 Third generation tsunami scenario matrix for the Portuguese Tsunami Early Warning
755 System. Proceedings of the 15 WCEE, Lisboa, Portugal,
756 <https://core.ac.uk/download/pdf/38626266.pdf>.

757 Melgar, D., Ruiz-Angulo, A., Garcia, E. S., Manea, M., Manea, V. C., Xu, X., ... & Ramirez-
758 Guzmán, L. (2018). Deep embrittlement and complete rupture of the lithosphere during the
759 M w 8.2 Tehuantepec earthquake. *Nature Geoscience*, 11(12), 955-960.

760 Mulia, I. E., Gusman, A. R., & Satake, K. (2018). Alternative to non-linear model for
761 simulating tsunami inundation in real-time. *Geophysical Journal International*, 214(3),
762 2002-2013.

763 Mulia, I. E., Gusman, A. R., & Satake, K. (2020). Applying a deep learning algorithm to
764 tsunami inundation database of megathrust earthquakes. *Journal of Geophysical Research:*
765 *Solid Earth*, 125(9), e2020JB019690.

766 National Emergency Management Agency [NEMA]. 2020. Tsunami advisory and warning
767 plan: supporting plan [SP 01/20]. Wellington (NZ): National Emergency Management
768 Agency; [accessed 2020 Aug 10].
769 [https://www.civildefence.govt.nz/assets/Uploads/publications-/Supporting-Plans/Tsunami-](https://www.civildefence.govt.nz/assets/Uploads/publications-/Supporting-Plans/Tsunami-Advisory-and-Warning-Plan-Supporting-Plan-Update-Jun-2020.pdf)
770 [Advisory-and-Warning-Plan-Supporting-Plan-Update-Jun-2020.pdf](https://www.civildefence.govt.nz/assets/Uploads/publications-/Supporting-Plans/Tsunami-Advisory-and-Warning-Plan-Supporting-Plan-Update-Jun-2020.pdf)

771 Neil, H., Orpin, A., Nodder, S., Mitchell, J., Northcote, L., Mackay, K., Kane, T. (2015). Large
772 Canyon-Channel Complexes from South Island of New Zealand Show Contrasting
773 Morphologies. AAPG Asia Pacific Region, Geoscience Technology Workshop, Modern
774 Depositional Systems as Analogues for Petroleum Reservoirs, April 21-22, 2015,
775 Wellington, New Zealand.
776 https://www.searchanddiscovery.com/abstracts/pdf/2015/90235gtw/abstracts/ndx_neil.pdf

777 Onat, Y., Yalciner, A.C. (2013). Initial stage of database development for tsunami warning
778 system along Turkish coasts. *Ocean Engineering*, 74, 141-154,
779 <https://doi.org/10.1016/j.oceaneng.2013.09.008>.

780 Okada, Y. (1985). Surface deformation due to shear and tensile faults in a half-space. *Bulletin*
781 *of the seismological society of America*, 75(4), 1135-1154.

782 Okal, E. A. (1988). Seismic parameters controlling far-field tsunami amplitudes: A review.
783 *Natural Hazards*, 1(1), 67-96.

784 Power, W., Wallace, L., Wang, X., & Reyners, M. (2012). Tsunami hazard posed to New
785 Zealand by the Kermadec and southern New Hebrides subduction margins: an assessment
786 based on plate boundary kinematics, interseismic coupling, and historical seismicity. *Pure*
787 *and applied geophysics*, 169(1), 1-36.

788 Power, W.L. (2017). A tool for Rapid Tsunami Threat (RTTM) generation. Lower Hutt, N.Z.:
789 GNS Science. *GNS Science report 2017/37*. 30 p.; doi: 10.21420/G2463J

790 Power, W.L.; Fry, B.; Gusman, A.R.; Burbidge, D.R.; Brewer, M.; Wang, X. 2018 DART
791 buoys network design. GNS Science consultancy report 2018/147. 53 p.

792 Reymond, D., Okal, E.A., Hébert, H., Bourdet, M. (2012). Rapid forecast of tsunami wave
793 heights from a database of pre- computed simulations, and application during the 2011
794 Tohoku tsunami in French Polynesia. *Geophysical Research Letters*, 39(11),
795 <https://doi.org/10.1029/2012GL051640>.

796 Roger, J., Pelletier, B. and Aucan, J. (2019). Update of the tsunami catalogue of New Caledonia
797 using a decision table based on seismic data and marigraphic records, *Natural Hazards and*
798 *Earth System Sciences*, 19, 1471-1483, <https://doi.org/10.5194/nhess-19-1471-2019>.

799 Roger, J., Pelletier, B., Duphil, M., Lefèvre, J., Aucan, J., Lebellegard, P., Thomas, B.,
800 Bachelier, C., Varillon, D. (2021). The Mw 7.5 Tadine (Maré, Loyalty Is.) earthquake and
801 related tsunami of December 5, 2018: implications for tsunami hazard assessment in New

802 Caledonia. *Natural Hazards and Earth System Sciences, Discussions*,
803 <https://doi.org/10.5194/nhess-2021-58>.

804 Romano, F., Piatanesi, A., Lorito, S., Tolomei, C., Atzori, S., & Murphy, S. (2016). Optimal
805 time alignment of tide- gauge tsunami waveforms in nonlinear inversions: Application to
806 the 2015 Illapel (Chile) earthquake. *Geophysical Research Letters*, 43(21), 11-226.

807 Rowden, A.A., Clark, M.R., Wright, I.C. (2005). Physical characterisation and a biologically
808 focused classification of “seamounts” in the New Zealand region. *New Zealand Journal of*
809 *Marine and Freshwater Research*, 2005, Vol. 39: 1039–1059. DOI:
810 10.1080/00288330.2005.9517374

811 Sahal A., Pelletier B., Chatelier J., Lavigne F. and Schindel  F.: A catalog of tsunamis in New
812 Caledonia from 28 March 1875 to 30 September 2009, *Comptes Rendus Geoscience*, 342,
813 437-444, 2010.

814 Satake, K. (1995). Linear and nonlinear computations of the 1992 Nicaragua earthquake
815 tsunami. *Pure and Applied Geophysics*, 144(3), 455-470.

816 Shepard, D. (1968, January). A two-dimensional interpolation function for irregularly-spaced
817 data. In *Proceedings of the 1968 23rd ACM national conference* (pp. 517-524).

818 Tanioka, Y., & Sataka, K. (1996). Fault parameters of the 1896 Sanriku tsunami earthquake
819 estimated from tsunami numerical modeling. *Geophysical Research Letters*, 23(13), 1549-
820 1552.

821 Tanioka, Y., Miranda, G. J. A., Gusman, A. R., & Fujii, Y. (2017). Method to determine
822 appropriate source models of large earthquakes including tsunami earthquakes for tsunami
823 early warning in Central America. *Pure and applied geophysics*, 174(8), 3237-3248.

824 Tatehata, H. (1997). The new tsunami warning system of the Japan Meteorological Agency.
825 In *Perspectives on Tsunami Hazard Reduction* (pp. 175-188). Springer, Dordrecht.

826 Titov, V.V., Moore, C.W., Greenslade, D.J.M. *et al.* A New Tool for Inundation Modeling:
827 Community Modeling Interface for Tsunamis (ComMIT). *Pure Appl. Geophys.* **168**, 2121–
828 2131 (2011). <https://doi.org/10.1007/s00024-011-0292-4>

829 Uruski, C. I. (2010). New Zealand's deepwater frontier. *Marine and Petroleum Geology*, 27(9),
830 2005-2026.

831 USGS, (2021). <https://earthquake.usgs.gov/earthquakes/eventpage/us6000dg77/executive>

832 Watada, S., Kusumoto, S., & Satake, K. (2014). Traveltime delay and initial phase reversal of
833 distant tsunamis coupled with the self-gravitating elastic Earth. *Journal of Geophysical*
834 *Research: Solid Earth*, 119(5), 4287-4310.

835 Wang X, Liu PLF. 2006. An analysis of 2004 Sumatra earthquake fault plane mechanisms and
836 Indian Ocean tsunami. *Journal of Hydraulic Research.* 44(2):147–154.
837 doi:10.1080/00221686.2006.9521671.

838 Wang X, Power WL. 2011. COMCOT: a tsunami generation, propagation and run-up model.
839 Lower Hutt (NZ): GNS Science. 121 p. (GNS Science report; 2011/43).

840 Wang, Y., Maeda, T., Satake, K., Heidarzadeh, M., Su, H., Sheehan, A. F., & Gusman, A. R.
841 (2019). Tsunami data assimilation without a dense observation network. *Geophysical*
842 *Research Letters*, 46(4), 2045-2053.

843 Yabuki, T., & Matsu'Ura, M. (1992). Geodetic data inversion using a Bayesian information
844 criterion for spatial distribution of fault slip. *Geophysical Journal International*, 109(2), 363-
845 375.

846

847